

1 Assimilation of multiple datasets results in large differences in 2 regional to global-scale NEE and GPP budgets simulated by a 3 terrestrial biosphere model

4
5 Cédric Bacour¹©, Natasha MacBean², Frédéric Chevallier¹, Sébastien Léonard¹*, Ernest N.
6 Koffi¹☆, Philippe Peylin¹

7 ¹ Laboratoire des Sciences du Climat et de l'Environnement, LSCE/IPSL, CEA-CNRS-UVSQ, Université Paris-Saclay,
8 Gif-sur-Yvette, F-91191, France.

9 ² Departments of Geography & Environment and Biology, Western University, London, Ontario, Canada.

10
11 © formerly at NOVELTIS, Labège, France.

12 * now at Air Liquide R&D, Innovation Campus Paris - Les-Loges-en-Josas, France.

13 ☆ now at European Centre for Medium-Range Weather Forecasts, Robert-Schuman-Platz 3, 53175 Bonn,
14 Germany.

15
16 *Correspondance to:* Cédric Bacour (cedric.bacour@lsce.ipsl.fr)

17 18 **Key Points:**

- 19 • The impact of assimilating different dataset combinations on regional to global scale C budgets
20 is explored with the ORCHIDEE model
- 21 • Assimilating simultaneously multiple datasets is preferable to optimize the values of the model
22 parameters and avoid model overfitting
- 23 • The challenges in constraining soil C disequilibrium using atmospheric CO₂ data are highlighted
24 for an accurate prediction of the land sink distribution

25 26 **Abstract**

27 In spite of the importance of land ecosystems in offsetting carbon dioxide emissions released by
28 anthropogenic activities into the atmosphere, the spatio-temporal dynamics of terrestrial carbon
29 fluxes remain largely uncertain at regional to global scales. Over the past decade, data assimilation
30 (DA) techniques have grown in importance for improving these fluxes simulated by Terrestrial
31 Biosphere Models (TBMs), by optimizing model parameter values while also pinpointing possible
32 parameterization deficiencies. Although the joint assimilation of multiple data streams is expected to

33 constrain a wider range of model processes, their actual benefits in terms of reduction in model
34 uncertainty are still under-researched, also given the technical challenges. In this study, we
35 investigated with a consistent DA framework and the ORCHIDEE-LMDz TBM-atmosphere model how
36 the assimilation of different combinations of data streams may result in different regional to global
37 carbon budgets. To do so, we performed comprehensive DA experiments where three datasets (*in*
38 *situ* measurements of net carbon exchange and latent heat fluxes, space-borne estimates of the
39 Normalized Difference Vegetation Index, and atmospheric CO₂ concentration data measured at
40 stations) are assimilated alone or simultaneously. We thus evaluated their complementarity and
41 usefulness to constrain net and gross C land fluxes. We found that a major challenge in improving the
42 spatial distribution of the land C sinks/sources with atmospheric CO₂ data relates to the correction of
43 the soil carbon imbalance.

44

45 **1 Introduction**

46

47 The dramatic growth of atmospheric CO₂ concentrations recorded in the last half-century has
48 increased awareness on the impact of human activities on climate. Taking up about one third of the
49 carbon dioxide from the atmosphere, the terrestrial biosphere plays a key role in regulating CO₂
50 emissions released by anthropogenic activities (fossil fuel emissions, land use and land cover change)
51 (Friedlingstein et al., 2020). Quantifying variations in the distribution and intensity of carbon (C)
52 sources/sinks from year to year remains a challenge given the complexity of the processes involved
53 and what we can learn from observations. By formalizing current knowledge of the main processes
54 governing the functioning of vegetation into numerical representations, terrestrial biosphere models
55 (TBMs) have grown in importance for studying the spatio-temporal dynamics of net and gross land
56 surface C fluxes from the local to the global scales. However, the large spread in simulated regional
57 to global scale C fluxes for the last few decade (Friedlingstein et al., 2020) as well as for future
58 projections (Arora et al., 2020) highlights the remaining uncertainties in our understanding and
59 prediction of the fate and role of the biosphere under climate change and anthropogenic pressure.

60

61 Over the past decade, the parameter uncertainty in TBMs has increasingly been reduced thanks to
62 statistical data assimilation (DA, also referred to as model-data fusion) frameworks, benefiting from
63 the experience gained in other fields of Earth and Environmental sciences (geophysics, weather
64 forecasting, hydrology, oceanography, etc.). DA techniques enable optimization of the model
65 parameters using relevant target observations, while taking into account both observational and
66 modelling uncertainties. DA does not only enable improving the model parameters but can also help

67 pinpointing model deficiencies (Luo et al., 2012). The importance of DA as a key component of
68 terrestrial biosphere carbon cycle modelling is reflected by the diversity of DA systems in the global
69 TBM communities. Since the first global scale Carbon Cycle Data Assimilation System (CCDAS)
70 (Kaminski et al., 2002; Rayner et al., 2005) developed for the Biosphere Energy-Transfer Hydrology
71 (BETHY) model, other modelling groups have developed their own global scale carbon cycle DA
72 systems, in particular for ORCHIDEE (ORganizing Carbon and Hydrology In Dynamic EcosystEms
73 model) (Santaren et al., 2007; Peylin et al., 2016), JULES (Joint UK Land Environment Simulator)
74 (Raoult et al. (2016)), JSBACH (Schürmann et al. (2016)), or CLM (Community Land Model) (Fox et al.,
75 2018), and in parallel to the development of community assimilation tools (as DART (Anderson et al.,
76 2009) or PECAn (Dietze et al. (2013))).

77

78 Within a variational DA framework, ground-based measurements of eddy-covariance fluxes at a local
79 scale (Wang et al., 2001; Knorr and Kattge, 2005; Sacks et al., 2007; Williams et al., 2009; Groenendijk
80 et al., 2011; Kuppel et al., 2012) have been widely used to constrain net and gross CO₂ fluxes and
81 latent heat flux. Moreover, remote sensing proxies of vegetation activities, such as raw reflectance
82 data (Quaife et al., 2008), vegetation indices (Migliavacca et al., 2009; MacBean et al., 2015), or
83 FAPAR - fraction of absorbed photosynthetically active radiation (Stöckli et al., 2008; Zobitz et al.,
84 2014; Forkel et al., 2014; Bacour et al., 2015), have also been used to constrain the model parameters
85 at various spatial scales. Finally, atmospheric CO₂ mole fraction measurements have been assimilated
86 to provide valuable information on large-scale net ecosystem exchange (NEE) (Rayner et al., 2005;
87 Koffi et al., 2012).

88

89 In the early days of DA studies, most focused on the assimilation of a single data stream (e.g.,
90 targetting only NEE). Then, assimilations with multiple C cycle related datasets have soon been
91 considered (Moore et al., 2008; Richardson et al., 2010; Ricciuto et al., 2011; Keenan et al., 2013;
92 Thum et al., 2017; Knorr et al., 2010; Kaminski et al., 2012; Kato et al., 2013; Bacour et al., 2015;
93 Peylin et al., 2016). The underlying motivation behind assimilating multiple data streams is that using
94 a greater number and diversity of observations should provide stronger constraints on model
95 parameters, including a wider range of processes, hence resulting in a greater reduction in model
96 uncertainty. However, many previous studies that assimilated multiple datasets hardly considered
97 potential incompatibilities between the model and the observations (although see Bacour et al., 2015;
98 Thum et al., 2017), that may result in a deterioration of model agreement with other observations
99 not included in the assimilation. Besides, only a few have quantified the actual benefit of assimilating
100 multiple data-sets compared to the single data stream assimilations, in particular in the context of
101 global scale C cycle DA experiments.

102 The assimilation of multiple data streams can be done either sequentially, in which one observation
103 type is assimilated at a time, or simultaneously (joint assimilation approach or “batch” strategy as
104 defined in Raupach et al., 2005), where the model is calibrated with all data included in the same
105 optimization (e.g. Richardson et al., 2010; Kaminski et al., 2012; Schürmann et al., 2016). Although
106 with model parameters and observations described by probability distributions, simultaneous and
107 sequential assimilations could theoretically lead to the same result (Tarantola et al., 2005), this is not
108 the case in practice for complex problems. Incomplete or incorrect description of the error statistics
109 may result in large differences between simultaneous and stepwise approaches (see Kaminski et al.,
110 2012; MacBean et al., 2016). In addition, model non linearities also tend to exacerbate these
111 potential differences. Simultaneous assimilation is considered to be more optimal in the context of
112 optimizing TBM parameters as it maximizes the consistency of the model with the whole of the
113 datasets considered (Richardson et al., 2010; Kaminski et al. 2012) and avoid incorrect/incomplete
114 propagation of the error statistics from one step to the other (Peylin et al., 2016). The use of a
115 gradient descent approach for the optimization, with the risk that it gets trapped in local minima,
116 also increases the chances that stepwise and simultaneous approaches diverge. However, sequential
117 approaches remain appealing for modelers: They require less initial technical investment and enable
118 easier assessment of the impact of each data stream assimilated successively onto the optimized
119 variables. Both approaches however face similar challenges, like defining the model-data uncertainty
120 (see, e.g., Richardson et al., 2010; Keenan et al., 2013; Kaminski et al., 2012; Bacour et al., 2015;
121 Thum et al., 2017; Peylin et al., 2016) and hence the weight that each dataset has on the
122 optimization outcome (although specific weighting approaches may be envisioned, as in Wutzler and
123 Carvalhais et al. (2014) or Oberpriller et al. (2021)) . Another major challenge, as highlighted by
124 MacBean et al. (2016) or Oberpriller et al. (2021), concerns inconsistencies between observations
125 and model outputs, which are usually not accounted for in common bias-blind (Dee, 2005) Bayesian
126 DA systems relying on the hypothesis of Gaussian errors. Indeed, most studies do not attempt to
127 identify systematic errors in the observations and/or in the model and to correct for them. The likely
128 impact of model-data biases on the parameter optimization is then a degraded model performance
129 as well as an illusory decrease in the estimated model uncertainty (Wutzler and Carvalhais, 2014;
130 MacBean et al., 2016; Bacour et al., 2019).

131
132 The present study aims to go a step forward in the assessment of how assimilating multiple C cycle
133 related data streams impacts and changes the constraint on net and gross CO₂ flux simulations at the
134 global scale. To do so, we further advance from the sequential assimilation of Peylin et al. (2016)
135 (referred to as “stepwise” approach hereafter) by implementing a simultaneous assimilation
136 framework with the same data streams: net carbon fluxes (net ecosystem exchange – NEE) and

137 latent heat fluxes (LE) measured at eddy covariance sites across different ecosystems, satellite
138 derived Normalized Difference Vegetation Index (NDVI) at coarse resolution for a set of pixels
139 spanning the main deciduous vegetation types, and monthly atmospheric CO₂ concentration data
140 measured at surface stations worldwide. The study relies on the variational DA framework designed
141 for the ORCHIDEE global vegetation model (Krinner et al., 2005), here associated to a simplified
142 version of the LMDz atmospheric transport model (Atmospheric General Circulation Model of the
143 Laboratoire de Météorologie Dynamique, Hourdin et al., (2006)) based on pre-calculated transport
144 fields for assimilating atmospheric CO₂ concentration data. ORCHIDEE and LMDz are the terrestrial
145 and atmospheric components of the Institut Pierre Simon Laplace (IPSL) Earth System Model
146 (Dufresne et al., 2013).

147 By conducting different assimilation experiments in which each data stream is assimilated alone or in
148 combination (for all combinations of datasets), the research questions that we address in this study
149 are:

150 1. What impact does the combination of different data streams assimilated have on the reduction
151 in model-data misfit, and to which extent are the model predictions improved (or degraded) with
152 respect to the other data-streams that were not assimilated?

153 2. How does the combination of different data-streams impact the optimised parameter values
154 and uncertainties, and the predicted spatial distribution of the net and gross carbon fluxes at
155 regional and global scales? How do the derived carbon budgets compare with independent
156 process-based model and atmospheric inversion estimates from the Global Carbon Project's 2020
157 Global Carbon Budget (Friedlingstein et al., 2020)?

158 3. How does a model–data bias related to incorrect initialisation of soil carbon pools (i.e. their
159 disequilibrium with respect to steady state) impact the overall optimisation performances within
160 a Bayesian assimilation framework relying on the hypothesis of Gaussian errors?

161 In addition, our analysis of the useful informational content provided by different data-streams on C
162 fluxes is supported by methodological aspects aiming to:

163 1. Improve the realism of the prior error statistics on parameters by making them consistent with
164 the prior model-data mismatch;

165 2. Quantify the observation influence of each of the three data streams on the joint assimilation in
166 which all three datasets were included in the optimization.

167 Throughout the presentation of the results, we discuss implications of each assimilation experiment
168 on our ability to accurately constrain gross and net CO₂ fluxes. In the final section we propose some
169 perspectives for other modeling groups wishing to implement global scale parameter DA systems to
170 constrain regional to global scale C budgets.

171

172 **2 Materials and methods**

173 **2.1 Models**

174 **2.1.1 ORCHIDEE**

175 Model description

176 ORCHIDEE is a spatially explicit process-based global TBM (Krinner et al. 2005) that calculates the
177 fluxes of carbon dioxide, water and heat, between the biosphere and the atmosphere, as well as the
178 soil water budget. The temporal resolution is half an hour except for the slow components of the
179 terrestrial carbon cycle (including carbon allocation in plant reservoirs, soil carbon dynamics, and
180 litter decomposition) which are calculated on a daily basis. The version of ORCHIDEE in this study
181 corresponds to that used in the IPSL Earth System Model for its contribution to the Climate Model
182 Intercomparison Project 5 (CMIP5) established by the World Climate Research Program
183 (<https://cmip.llnl.gov/>). Vegetation is represented by 13 Plant Functional Types (PFTs) that include
184 bare soil. The processes use the same governing equations for all PFTs, except for the seasonal leaf
185 dynamics (phenology), which follows Botta et al. (2000) (see MacBean et al. (2015) for a full
186 description). The observation operator for NDVI is determined *i*) by assuming a linear relationship
187 between NDVI and FAPAR (Myneni et al., 1994) and *ii*) by calculating FAPAR from the simulated LAI
188 based on the classical Beer-Lambert law for the extinction of the direct illumination within the
189 canopy (Bacour et al., 2015; MacBean et al., 2015). In addition, we consider normalized data in our
190 assimilation scheme. The soil organic carbon is simulated by a CENTURY-type model (Parton et al.,
191 1987) and is partitioned in three pools (slow, passive, active) with different residence times.

192

193 Model Set-up

194 The set-up of the simulations performed with ORCHIDEE depends on the data assimilated. The model
195 is run at site scale for the assimilation of eddy-covariance measurements, at a spatial resolution of
196 0.72° for the assimilation of the satellite NDVI data, and at the resolution of the atmospheric
197 transport model LMDz (3.75°x2.5°) for the assimilation of atmospheric CO₂ measurements. The Olson
198 land cover classification at 5 km is used to derive the PFT fractions at each spatial resolution, but for

199 the flux tower simulations where the proportion of each PFT is set based on expert knowledge. For
200 satellite pixels and global simulations, ORCHIDEE is forced using the 3-hourly ERA-Interim gridded
201 meteorological forcing fields (Dee et al., 2011) (aggregated at $3.75^{\circ} \times 2.5^{\circ}$ when assimilating
202 atmospheric CO_2 concentrations). For the flux tower simulations, the model is forced by local
203 measurements of the meteorological variables at a half-hourly time step.

204 For each spatial resolution, a prior spin-up simulation was performed by recycling available forcing
205 data. The objective was to bring the different soil carbon reservoirs to “realistic” values, albeit the
206 spin-up runs result in neutral net carbon flux by construction. Each spin-up simulation was then
207 followed by a transient simulation (starting from the first year of measurement for each data stream)
208 and accounting for the secular increase of atmospheric CO_2 concentrations; for the global simulations,
209 only a short transient simulation from 1990 to 1999 was performed.

210

211 **2.1.2 LMDz**

212 Model description

213 The study relies on version 3 of LMDz (Hourdin et al., 2006) as implemented for the IPSL contribution
214 to CMIP4. In order to save computational time, we used LMDz in the form of a precomputed
215 Jacobian matrix at a set of CO_2 measurement stations (§2.2.3) (see details in Peylin et al., 2016).

216

217 Model set-up

218 To simulate atmospheric CO_2 concentrations that can be compared to observations, the transport
219 model has to be forced not only by terrestrial biospheric fluxes (calculated by ORCHIDEE), but also by
220 other natural (e.g. ocean) and anthropogenic CO_2 fluxes. We imposed a net emission due to land use
221 change (i.e. deforestation) of 1.1 GtC.yr^{-1} although we also accounted for a larger flux from biomass
222 burning but compensated partly by forest regrowth (see Peylin et al. (2016) for more details). The
223 global maps of biomass burning emissions were taken from the Global Fire Emission Database
224 version 3 dataset (Van der Werf et al., 2006; Randerssen et al., 2013) over the period 1997-2010 at a
225 monthly time step and gridded at $0.5^{\circ} \times 0.5^{\circ}$ resolution. The global fossil fuel CO_2 emission products
226 used here were developed by University of Stuttgart/IER based on EDGAR v4.2 and were provided at
227 a $0.1^{\circ} \times 0.1^{\circ}$ spatial resolution and at a monthly time scale. The ocean flux component was obtained
228 from a data-driven statistical model based on artificial neural networks that estimated the spatial
229 and temporal variations of the air-sea CO_2 fluxes (Peylin et al., 2016).

230

231 **2.2 Assimilated data**

232 **2.2.1 in situ flux measurements (F)**

233 The NEE and LE measurements come from the FLUXNET global network. We used harmonized,
234 quality-checked and gap-filled data (Level 4) at 68 sites from the La Thuile global synthesis dataset
235 (Papale, 2006). The site locations are presented in Figure 1. These ecosystem measurements cover
236 very different time spans, ranging from one single year at some sites up to nine years. They constrain
237 seven PFTs among the twelve natural vegetation types represented in ORCHIDEE: tropical evergreen
238 broadleaf forest – TrEBF (3 sites corresponding to 6 site-years), temperate evergreen needleleaf
239 forest – TeENF (16 sites, 45 sites-years), temperate evergreen broadleaf forest – TeEBF (2 sites, 4
240 site-years), temperate deciduous broadleaf forest – TeDBF (11 sites, 37 site-years), boreal evergreen
241 needleleaf forest – BoENF (12 sites, 44 site-years), boreal deciduous broadleaf forest – BoDBF (3 sites,
242 6 site-years), and C3 grassland – C3GRA (21 sites, 56 site-years). We assimilated daily-mean values of
243 NEE and LE observations, but only when at least 80% of the 48 potential half-hourly data in a day are
244 available.

245 **2.2.2 Satellite products (VI)**

246 The NDVI products considered here are derived from MODIS collection 5 surface reflectance data
247 acquired in the red and near-infrared channels and corrected from the directional effects (Vermote
248 et al. (2008). Data already assimilated into ORCHIDEE and described in MacBean et al. (2015) are
249 considered here: They are provided at daily / 0.72° resolutions and span over the 2000-2010 period.
250 Five among the six deciduous, non-agricultural, PFTs of ORCHIDEE were optimized in this study:
251 TrDBF - tropical broadleaved rainy green forest, TeDBF, BoDBF, BoDNF – Boreal needleleaf
252 summergreen forest, and C3GRA. C4 grasses and evergreen PFTs were not considered. For each PFT,
253 fifteen 0.72° pixels were selected for assimilation depending on their thematic homogeneity with
254 respect to the considered PFT (fractional coverage above 60%) and consistency between the
255 observed NDVI time series and the prior ORCHIDEE. The location of these satellite pixels is shown in
256 Figure 1.

257

258 **2.2.3 Atmospheric CO₂ measurements (CO₂)**

259 The surface atmospheric CO₂ concentration data come from three databases: The NOAA Earth
260 System Laboratory (ESRL) archive (<ftp://ftp.cmdl.noaa.gov/ccg/co2/>), the CarboEurope IP project
261 (http://ceatmosphere.lsce.ipsl.fr/database/index_database.html), and the World Data Centre for
262 Greenhouse Gases of the World Meteorological Organization Global Atmospheric Watch Programme
263 (<http://gaw.kishou.go.jp>). The data include *in situ* measurements, made by automated quasi-

264 continuous analysers, and air samples collected in flasks and later analyzed at central facilities. In this
 265 study, we used monthly-mean values of these measurements (Peylin et al., 2016). Ten years of
 266 observations over the 2000-2009 period were used from a total of 53 stations located around the
 267 world (Figure 1).

268

269 **2.3 Assimilation methodology**

270 **2.3.1 Data assimilation framework**

271 The data assimilation system associated to the ORCHIDEE model (ORCHIDAS) has been described in
 272 previous studies regarding the assimilation of these data streams alone (Kuppel et al., 2012; Santaren
 273 et al., 2014; MacBean et al., 2015; Bastrikov et al., 2018) or their combinations (Bacour et al., 2015;
 274 Peylin et al., 2016). The assimilation system relies on a variational Bayesian framework that optimizes
 275 ORCHIDEE parameters gathered in a vector \mathbf{x} , by finding the minimum of a global misfit function $J(\mathbf{x})$
 276 iteratively. $J(\mathbf{x})$ is a linear combination of the misfit functions associated with each data stream. It is
 277 assumed that the errors of observations and on the model parameters are Gaussian and that the
 278 data streams errors are independent from each other:

279

$$J(\mathbf{x}) = \frac{1}{2} [(H_{LMDz} \circ H_{ORCH}(\mathbf{x}) - \mathbf{y}^{CO2})^T \cdot \mathbf{R}_{CO2}^{-1} \cdot (H_{LMDz} \circ H_{ORCH}(\mathbf{x}) - \mathbf{y}^{CO2}) + \quad (1)$$

$$(H_{ORCH}(\mathbf{x}) - \mathbf{y}^F)^T \cdot \mathbf{R}_F^{-1} \cdot (H_{ORCH}(\mathbf{x}) - \mathbf{y}^F) + (H_{ORCH}(\mathbf{x}) -$$

$$\mathbf{y}^{VI})^T \cdot \mathbf{R}_{VI}^{-1} \cdot (H_{ORCH}(\mathbf{x}) - \mathbf{y}^{VI}) + (\mathbf{x} - \mathbf{x}^b)^T \cdot \mathbf{B}^{-1} \cdot (\mathbf{x} - \mathbf{x}^b)]$$

280

281 where \mathbf{y}^o are the observation vectors (with $o = F$ (flux), VI (satellite NDVI), or $CO2$ (CO_2 concentration));
 282 H_{ORCH} and H_{LMDz} are the observational operators of the ORCHIDEE and LMDz models, respectively. \mathbf{R}_o
 283 is the error covariance matrix characterizing the observation errors with respect to the model
 284 (therefore including the uncertainty in the model structure) associated to data stream o . The
 285 dimensionless control vector \mathbf{z} quantifies the distance between the values of the optimized
 286 parameters and the corresponding prior information \mathbf{x}^b : $\mathbf{z} = \mathbf{B}^{-1/2} \cdot (\mathbf{x} - \mathbf{x}^b)$, where \mathbf{B} is the
 287 associated *a priori* error covariance matrix.

288 We use the gradient-based L-BFGS-B algorithm (Byrd et al., 1995; Zhu et al., 1997) to minimize $J(\mathbf{x})$
 289 iteratively. It accounts for bounds in the parameter variations. The algorithm requires the gradient of
 290 the misfit function as an input in order to explore the parameter space:

291

$$\nabla_{\mathbf{x}} J(\mathbf{x}) = \mathbf{H}_{ORCH}^{CO2 T} \cdot \mathbf{H}_{LMDz}^T \cdot \mathbf{R}_{CO2}^{-1} \cdot (H_{LMDz} \circ H_{ORCH}(\mathbf{x}) - \mathbf{y}^{CO2}) + \quad (2)$$

$$\mathbf{H}_{ORCH}^F T \cdot \mathbf{R}_F^{-1} \cdot (H_{ORCH}(\mathbf{x}) - \mathbf{y}^F) + \mathbf{H}_{ORCH}^{VI T} \cdot \mathbf{R}_{VI}^{-1} \cdot (H_{ORCH}(\mathbf{x}) - \mathbf{y}^{VI}) +$$

$$\mathbf{B}^{-1} \cdot (\mathbf{x} - \mathbf{x}^b)$$

292

293 The calculation of $\nabla_{\mathbf{x}} J(\mathbf{x})$ uses the Jacobian matrix of ORCHIDEE associated to each data stream,
294 $\mathbf{H}_{\text{ORCH}}^{\circ}$ (assuming local linearity of the model), and that of LMDz. For most of ORCHIDEE
295 parameters, $\mathbf{H}_{\text{ORCH}}^{\circ}$ (or \mathbf{H}° in hereafter) is calculated thanks to the tangent linear model of
296 ORCHIDEE obtained by automatic differentiation using the TAF (Transformation of Algorithms in
297 Fortran) tool (Giering et al., 2005); however, for a few parameters involved in threshold conditions of
298 the model processes, especially related to phenology, we use a finite difference method.

299

300 After optimization, the posterior error covariance matrix \mathbf{A} (for “analysis”) of the optimized
301 parameters can be calculated as a function of the Jacobian matrix associated to the gradients of the
302 model outputs with respect to the parameters at the solution for each data stream:

303

$$\mathbf{A} = \left[\sum \mathbf{H}^{\circ \text{T}} \cdot \mathbf{R}_o^{-1} \cdot \mathbf{H}^{\circ} + \mathbf{B}^{-1} \right]^{-1} \quad (3)$$

304

305 It is computed under the hypothesis of model linearity in the vicinity of the solution. The square root
306 of the diagonal elements of \mathbf{B} or \mathbf{A} correspond to the standard deviation σ on model parameters.

307 **2.3.2 Parameters to be optimized**

308

309 We chose to optimize a limited set of carbon-cycle related parameters of ORCHIDEE as a result of
310 preliminary sensitivity analyses and past DA studies. A short definition of these parameters that
311 mostly control photosynthesis, phenology and respiration, is provided in Table 1, while their
312 associated prior values, bounds and uncertainty are documented in Supplementary Table S3. More
313 comprehensive descriptions of their role in the model processes are provided in Kuppel et al. (2012)
314 and MacBean et al. (2015). The size of soil carbon pools drives the magnitude of the net carbon
315 fluxes exchanged with the atmosphere to a large extent; Soil carbon is closely related to soil texture,
316 climatic (temperature and moisture), disturbance history (including land use and fires), as well as
317 ecosystem and edaphic properties (Schimel et al., 1994; Todd-Brown et al., 2013) . Given that we do
318 not have access to that information, neither at the site scale (for assimilation of NEE measurements)
319 nor at the global scale (for assimilation of atmospheric CO₂ concentrations), we use a steady state
320 assumption where ORCHIDEE has been brought to near equilibrium with a long spin-up of the soil
321 carbon pools. To correct for this bias, the initial state of the soil carbon reservoirs is optimized using a
322 multiplicative parameter of both the slow and passive pools as in Peylin et al.(2016). The use of these
323 correction factors is a handy way to correct any issues related to the use of our soil organic C model

324 and the soil carbon disequilibrium. Two multiplicative parameters are used depending on the type of
325 data considered (and their associated spatial scale): for *in situ* flux measurements, we considered
326 site-specific parameters $K_{soilC,site}$; for atmospheric CO₂ concentration data, instead of resolving the
327 initial conditions for all LMDz grid cells we scaled the carbon pools for 30 large scale regions $K_{soilC,reg}$.
328 Note that having correct soil carbon pools is less important when assimilating satellite NDVI data
329 because these are more closely related to carbon uptake rather than net carbon flux. In total, up to
330 182 parameters are optimized depending on the data streams considered.

331 The prior values x^b of the parameters are set to the standard values of ORCHIDEE (Supplementary
332 Table S3). Not all parameters are constrained by all three data streams. In particular, satellite
333 FAPAR/NDVI products inform the timing of phenology of plant vegetation (start and end of the
334 growing season) rather than on photosynthesis or respiration with our DA system (Bacour et al., 2015;
335 MacBean et al., 2015). The dependency of each parameter with respect to the assimilated data
336 streams is indicated in Table 1.

337

338 **2.3.3 Data assimilation experiments**

339 Different data assimilation experiments were tested in order to understand the respective constraint
340 brought by each data stream and evaluate their compatibility with each other and with the model.
341 First, each data stream was assimilated separately and then its combinations with the other two
342 were considered. Second, the three data streams were assimilated altogether. The various
343 experiments are described in Table 2 with the number of data points assimilated and the number of
344 parameters optimized. Indeed, the number of optimized parameters differs with the type of data
345 assimilated as described in §2.3.2 and in Table 1. The assimilations have a high computational cost,
346 with an average value for joint assimilations using all three data streams of about 50,000 hr Central
347 Processing Unit time on AMD Rome compute nodes at 2.6 GHz with 256 GB memory per node.

348 Two assimilation experiments combining the three data streams were tested: one experiment
349 (F+VI+CO₂) with all parameters optimized in a single step; and an additional experiment following a
350 2-step optimization (F+VI+CO₂-2steps), as described hereafter. In the first step, the global soil carbon
351 reservoirs were constrained by assimilating atmospheric CO₂ data only, and optimizing the two main
352 parameters controlling soil respiration, $K_{soilC_{reg}}$ and $Q10$. In the second step, all parameters but
353 $K_{soilC_{reg}}$ were optimized from the three data streams: $K_{soilC_{reg}}$ was retained from the first step and
354 $Q10$ was optimized but the prior uncertainty for $Q10$ for the second step corresponded to the
355 posterior uncertainty derived from the first step. We did this to correct for the initialisation of the
356 soil carbon imbalance following model spin-up and illustrate how the informational content of the
357 three data-streams relative to the surface carbon fluxes can be enhanced once soil carbon

358 disequilibrium is more “realistically” represented; the motivations and implications of the two
359 assimilations experiments are further discussed in the result and discussion sections.

360 The results of these assimilations were compared to the companion study of Peylin et al. (2016) in
361 which the same data streams were assimilated in a sequential/stepwise approach: NDVI data were
362 assimilated first, then *in situ* flux measurements, and finally atmospheric CO₂ concentration
363 measurements. While only 3 years of atmospheric CO₂ data were used in Peylin et al. (2016), the
364 stepwise results presented here really accounts for the same ten years used in the simultaneous
365 experiments (2000-2009) to facilitate the comparison of the approaches (in particular the impact of
366 using the atmospheric CO₂ growth rate over 10 years on the optimisation of the mean terrestrial
367 carbon sink). There are however a few differences in the set-up compared to the present study (cf.
368 details provided in Supplementary Text S1).

369

370 **2.3.4 Error statistics on observations and parameters**

371 **2.3.4.1 Observation error statistics**

372 Like in previous studies with ORCHIDAS, we defined \mathbf{R}_o as diagonal and computed the variances
373 from the Root Mean Square Difference (RMSD) between the data and the *a priori* ORCHIDEE
374 simulations (*i.e.* performed with the model default parameter values) for fluxes and satellite
375 observations. However, it is worth noting that this approach overestimates the variances in order to
376 compensate for any neglected correlations. For atmospheric CO₂ measurements, we followed a
377 different methodology given the large discrepancy in the modelled *a priori* concentrations with
378 respect to the observed data (*i.e.*, large bias that increases over time due to biases in the land net
379 carbon sink (too small)). The errors were determined at each site as the standard deviation of the
380 observed temporal concentrations (Peylin et al., 2005, 2016), to capture the general feature that
381 model-data mismatch is likely large for sites and months with large variations in daily concentrations.
382 Although crude, such an hypothesis has been used in many atmospheric CO₂ inversions and in our
383 case it combines all structural errors of the terrestrial and transport models.

384

385 **2.3.4.2 Tuning of the prior error statistics**

386 We assumed that errors in the prior parameter values are independent and therefore we used a
387 diagonal \mathbf{B} matrix. We populated the diagonal of \mathbf{B} in an iterative way from consistency diagnostics of
388 the data assimilation system following Desroziers et al. (2005), as described hereafter. If both \mathbf{B} and
389 \mathbf{R}_o matrices are correctly specified and if the estimation problem is linear, they should be related to

390 the covariance of the residuals (\mathbf{d}) between observations and background simulations (*i.e.* innovation)
 391 following:

$$\mathbf{H}^o \cdot \mathbf{B} \cdot \mathbf{H}^{oT} + \mathbf{R}_o = E [(\mathbf{y}^o - H(\mathbf{x}^b)) \cdot (\mathbf{y}^o - H(\mathbf{x}^b))^T] = E [\mathbf{d}_b^o \cdot \mathbf{d}_b^{oT}] \quad (4)$$

392

393 With

$$\mathbf{R}_o = E [(\mathbf{y}^o - H(\mathbf{x}^a)) \cdot (\mathbf{y}^o - H(\mathbf{x}^b))^T] = E [\mathbf{d}_a^o \cdot \mathbf{d}_b^{oT}] \quad (5)$$

394

$$\mathbf{H}^o \cdot \mathbf{B} \cdot \mathbf{H}^{oT} = E [(H(\mathbf{x}^a) - H(\mathbf{x}^b)) \cdot (\mathbf{y}^o - H(\mathbf{x}^b))^T] = E [\mathbf{d}_b^a \cdot \mathbf{d}_b^{oT}] \quad (6)$$

395

396 Similarly, the diagnostic on analysis errors can be determined from the residuals between
 397 observations and posterior simulations as:

$$\mathbf{H}^o \cdot \mathbf{A} \cdot \mathbf{H}^{oT} = E [(H(\mathbf{x}^a) - H(\mathbf{x}^b)) \cdot (\mathbf{y}^o - H(\mathbf{x}^a))^T] = E [\mathbf{d}_b^a \cdot \mathbf{d}_a^{oT}] \quad (7)$$

398

399 In principle, the tuning of \mathbf{B} and \mathbf{R} needs to be performed iteratively for successive values of \mathbf{x}^a and
 400 of the corresponding residuals, until convergence, which is prohibitive in terms of computing time.
 401 The estimation of the covariance matrices depends on the mathematical expectation (E) which would
 402 require several realizations of the residuals to diagnose the error statistics (Desroziers et al. (2005);
 403 Cressot et al., 2014). In this study, only one optimization was performed using one set of *a priori*
 404 parameters for each dataset. We therefore calculated these metrics by averaging the diagonals of
 405 the matrices described by both sides of the equations for all available observations (Kuppel et al.,
 406 2013). This way, both sides are scalar values (Cressot et al., 2014).

407

408 The standard deviation of the errors were determined after a few trials considering the three single
 409 data stream assimilation experiments independently: For each DA experiment we started from an
 410 initial parameter error set at 40% of the variation interval for each parameter (as in Peylin et al.,
 411 2016); The errors were then varied in order to fulfill the consistency diagnostics on the parameter
 412 and observation errors (see Supplementary Text S3). Finally, we evaluated the consistency of the
 413 resulting model-data covariance matrices for the DA experiments with multiple data streams using
 414 the reduced chi-square test (*i.e.* the chi-square statistic normalized by the number of observations, m
 415 (Chevallier et al., 2007; Klonecki et al., 2012), which is implicitly optimized by the Desroziers et al.
 416 (2005) approach:

$$\chi^2 = \frac{2J(\mathbf{x}^a)}{m} \quad (8)$$

417

418 If the \mathbf{R}_o and \mathbf{B} covariance matrices are well defined, the ratio of each term of the diagnostics of
419 Desroziers et al. (2005) (ratio between \mathbf{R}_o and $E[\mathbf{d}_a^o \cdot \mathbf{d}_b^{oT}]$; $\mathbf{H}^o \cdot \mathbf{B} \cdot \mathbf{H}^{oT}$ and $E[\mathbf{d}_b^a \cdot \mathbf{d}_b^{oT}]$; and
420 $\mathbf{H}^o \cdot \mathbf{B} \cdot \mathbf{H}^{oT} + \mathbf{R}_o$ and $E[\mathbf{d}_b^o \cdot \mathbf{d}_b^{oT}]$) should approach 1. Table 3 shows the values of the
421 consistency diagnostics for the final parameter error set-up.

422 The diagnostics for \mathbf{R}_o (ratios slightly above 1 for all data streams) and for the reduced chi-square
423 (Table S1 - values below 1) indicates a slight overestimation of the observation error. The diagnostics
424 for \mathbf{B} (*ratio^B*) show a stronger overestimation of the *a priori* error for NEE, LE and atmospheric CO₂,
425 but an underestimation for NDVI. For fluxes and satellite data, the combined diagnostics for \mathbf{R}_o and
426 \mathbf{B} (*ratio^{BR}*) appear consistent with ratios close to 1. For CO₂ however, the value of *ratio^{BR}* close to the
427 value of *ratio^B* highlights the strong influence of the background information (\mathbf{B} matrix) or the model
428 structure on the optimization, while the large value of χ^2 expresses a strong underestimation of the
429 observation error. Indeed, when determining \mathbf{R}_{CO_2} , we purposely did not account for the large bias (by
430 about 1 ppm.yr⁻¹) between the observed CO₂ temporal profiles at stations and the prior simulations,
431 which is due to the initialisation of ORCHIDEE's carbon pools (which is discussed in the Result section).
432 Finally, for the diagnostics on the analysis, the various tests performed (Supplementary Text S3) all
433 lead to negative quantities. Instead, the simulations of the calibrated model were expected to be
434 contained in between their prior state and the observations (the residuals having opposite signs,
435 their product is positive). This result may reflect a too strong model correction. However, it should be
436 noted that a strong assumption associated with these tests concerns the linearity of the model,
437 which may not hold for terrestrial biosphere models.

438

439 **2.4 Diagnostics for system evaluation**

440 **2.4.1 Optimisation performance**

441 We measured the efficiency of any assimilation by quantifying the reduction of the cost function as
442 the ratio of the prior to posterior values. It should be noted that the minimum value of the cost
443 function is not expected to be zero given the uncertainty in both the data and model, and the limited
444 number of degrees of freedom (number of optimized parameters) allowed. We also looked at the
445 ratio of the norm of the gradient between the prior and posterior misfit functions, as it illustrates the
446 progression towards the expected optimum, for which the gradient is null. The decrease of the norm
447 of the gradient depends on the estimation problem (non-linearities, number of observations versus
448 number of optimized parameters, constraints of the data on the model processes, etc.); However,
449 based on our experience with non-linear problems, we still expect the norm of the gradient to be
450 reduced by at least two orders of magnitude.

451 The analysis of the optimization performances are summarized in §3.1 and detailed in
452 Supplementary Text S4.

453

454 **2.4.2 Model improvement and posterior predictive checks**

455 The model improvement was quantified by the reduction of the RMSD between model and data,
456 prior and posterior to optimization, expressed in %, as $100 \times (1 - \text{RMSD}_{\text{post}}/\text{RMSD}_{\text{prior}})$.

457 We conducted posterior predictive checks by running the model optimized after assimilation of one
458 or two data streams and quantifying the resulting model-improvement with respect to the data
459 streams not accounted for in the assimilation.

460 **2.4.3 Uncertainty reduction on parameters and error budget**

461 The knowledge improvement on the model parameters brought by assimilation was assessed by the
462 uncertainty reduction determined by $1 - \sigma_{\text{post}}/\sigma_{\text{prior}}$, where σ_{post} and σ_{prior} are the standard deviation
463 derived from the posterior (**A**) and prior (**B**) covariance matrices on the model parameters and
464 output variables.

465 A comprehensive quantification of the uncertainty reduction on model variables would require
466 accounting also for the covariance matrix of the model structural error which could be the dominant
467 factor. Because this covariance matrix is difficult to estimate for complex process-based terrestrial
468 biosphere models (see Kuppel et al., 2013, for a first attempt in the case of the NEE), we instead
469 analyzed the posterior errors on NEE and GPP at regional to global scales, as the projection of the
470 posterior error on parameters in the space of the model variables. The posterior error on C fluxes is
471 then characterized by the covariance matrix \mathbf{R}^a as:

$$\mathbf{R}^a = \mathbf{H}^o \cdot \mathbf{A} \cdot \mathbf{H}^{oT} \quad (9)$$

472 with the Jacobian matrix \mathbf{H}^o , being the first derivative of the target quantity (e. g., NEE, GPP) to the
473 optimized parameters derived from an assimilation experiment o .

474

475 **2.4.4 Assessment of the information content of each data stream**

476 For the joint assimilations using the three different data streams, we further analyzed the influence
477 matrix \mathbf{S} that quantifies their leverage on the model-data fit (Cardinali et al., 2004):

$$\mathbf{S} = \mathbf{R}^{-1} \cdot \mathbf{H}^o \cdot \mathbf{A} \cdot \mathbf{H}^{oT} \quad (10)$$

478

479 A diagonal element S_{ii} is the rate of change of the simulated observable i with respect to variations in
480 the corresponding assimilated observation i . S_{ii} is referred to as "self-sensitivity" of "self-influence". A
481 zero self-sensitivity indicates that this i^{th} observation does not contribute to improving its simulation

482 by the model, whilst $S_{ij} = 1$ indicates that the fit of the sole observation i mobilizes an entire degree of
483 freedom (*i.e.* one parameter). In addition to the total influence matrix (equation 10), we also
484 determined the partial influence matrices associated to each data stream o , using the corresponding
485 diagonal \mathbf{R}_o matrices and in equation 10.

486 We analyzed the trace (*i.e.* the sum of all diagonal elements) of \mathbf{S} that quantifies a measure of the
487 amount of information that can be extracted from all observations / all data streams. We used two
488 derived quantities: the global average observation influence (OI) and the relative degrees of freedom
489 for signal (DFS) associated with the data stream o , which measures its relative contribution to the fit.
490 They are defined as follow (with m the total number of observations):

491

$$OI = \frac{tr(\mathbf{S})}{m} \quad (11)$$

492 and

$$DFS = 100 \times \frac{tr(\mathbf{S}_o)}{tr(\mathbf{S})} \quad (12)$$

493 **3 Results**

494 **3.1 Model improvement for the different assimilation experiments**

495 **3.1.1 Cost function reduction**

496 The reduction of the cost function varies between the different experiments with the lowest
497 reductions for the single data streams experiments F and VI (around 10%). However, the correction
498 of the model-data misfit when CO₂ data are assimilated is much higher (at least factor of 10
499 reduction). Noteworthy, this strong model improvement is obtained for a lower departure of the
500 parameters from their prior values than when fluxes or satellite data are assimilated (*cf.* section 3.3,
501 and Figure 6).

502 A detailed description of the optimization performances with respect to the minimisation of the cost
503 function is detailed in Supplementary Text S4 and Table S2.

504 **3.1.2 Overall fit to the observations**

505 The impact of assimilating one type of observation on all the data streams (including those that are
506 not assimilated) was evaluated for the various assimilation experiments. The reduction of the model-
507 data mismatch (*i.e.* reduction in prior RMSD) after assimilation of each data stream (or any
508 combination of them) is illustrated in Figure 2. The length of the boxes (first and third quartiles) of
509 the whisker plots highlight the spread in misfit reduction across sites/vegetation types. For fluxes,
510 only the impact on NEE is shown, given the choice of optimizing parameters is mostly related to the
511 carbon cycle. Using the parameter values optimized in either the F and VI assimilations has a strong

512 detrimental impact on the simulated atmospheric CO₂ data because the soil carbon pools were not
513 adjusted in these DA experiments. Therefore, we also analyzed the changes induced on the
514 detrended seasonal cycles of atmospheric CO₂ concentrations (Figure 2c) (hence removing the trend
515 using the time series decomposition based on the CCGCRV routine (Thoning et al., 1989 - see
516 Supplementary text S2 and Figure S1 for representative comparisons of observed vs modeled time
517 series of atmospheric CO₂ concentrations and their associated trend estimation).

518

519 For a given data stream, the improvement is usually better for the experiment where that data
520 stream is assimilated alone. One noteworthy exception is the assimilation of NDVI alone (VI
521 experiment where only the phenology parameters are optimized) that results in a lower model
522 improvement with respect to NDVI than when it is assimilated in combination with other data-
523 streams (where a higher number of parameters are optimized in these joint assimilations, hence
524 improving the timing of phenology and the amplitude of the annual cycle when flux or atmospheric
525 CO₂ data are also assimilated). For both experiments F and VI, the reduction of the model-data misfit
526 can be negative, which reflects how the assimilation can degrade the model performance for a few
527 pixels/sites by searching for a common parameter set. This is not observed with the assimilation of
528 atmospheric CO₂ data only for which the optimized model is always closer to the observations than
529 the prior model (due to a correction of the CO₂ trend), at all stations (see Supplementary Text S5 for
530 a detailed description of the reduction in model-data misfit for each single-data stream assimilation
531 experiment (F, VI, CO₂)).

532

533 The collateral impact of assimilating one data stream on the other simulated observables is evident
534 in the misfit reductions shown in Figure 2 (e.g., examine the “VI” experiment on the NEE misfit
535 reduction in Figure 2a). While using optimized phenological parameters retrieved from satellite data
536 alone (experiment VI) degrades the modelled seasonality of NEE as compared to the measurements
537 (median RMSD reduction of -3%), the optimization with respect to *in situ* flux data (F), with additional
538 control parameters, leads to a general improved consistency between modelled FAPAR and satellite
539 NDVI time series (median RMSD reduction of 8%). The impact on LE is much lower for all DA
540 experiments (median values close to 0% in all cases, result not shown). One can also note the
541 positive impact of the F and VI assimilations on the atmospheric CO₂ data with median RMSD
542 reductions of 15.8% and 11.2% respectively for the detrended time series. Such an improvement
543 after assimilation of *in situ* flux data corroborates the findings of Kuppel et al. (2014) and Peylin et al.
544 (2016). Noteworthy, this improvement is of the same order as that achieved when assimilating
545 atmospheric CO₂ data alone (median RMSD reduction of 14%). The parameters retrieved from the

546 CO₂ experiment have also a small but positive impact at the site level with respect to NEE (median
547 value of 3%) and FAPAR (0.8%).

548 For the joint assimilation experiment (F+VI, F+CO₂, VI+CO₂, or F+VI+CO₂; Figure 2), the model-data
549 agreement is improved for all assimilated data streams, as expected, while the model degradation
550 relative to the data not assimilated is generally not as severe as compared to the assimilation of
551 individual data stream experiments described above, with the exception of the F+VI experiment. The
552 latter experiment leads to enhanced model improvement compared to when flux and satellite NDVI
553 data are assimilated alone (cf. Supplementary Text S5). In the simultaneous assimilations involving
554 atmospheric CO₂ data, most of the model improvement concerns CO₂ (Figure 2c) while the benefit
555 for the fluxes and FAPAR/NDVI is weak (RMSD reduction below 3%). Noteworthy, the 2-step
556 assimilation F+VI+CO₂ (see Section 2.3.3) results in an even higher model improvement for both NEE
557 and FAPAR than the 1-step approach.

558 The misfit reduction for the raw (i.e., not detrended) atmospheric CO₂ data is high (median reduction
559 ~75%) and remains quite stable among the various different combinations of data streams that
560 include atmospheric CO₂ (Figure 2c solid bars experiments including "CO₂"), with the exception of
561 the F+VI+CO₂-2steps experiments. The misfit reductions for the detrended CO₂ time series are
562 generally lower (median reduction less than ~15%) and there are more pronounced differences
563 between experiments.

564 These results and the low reduction in NEE and FAPAR RMSDs following the assimilation atmospheric
565 CO₂ data described above highlight the predominance of the correction of the trend in atmospheric
566 CO₂ time series through the fitting of the carbon pool parameters, over the tuning of the other model
567 parameters related to photosynthesis and phenology (see Figure 6 and Figure S3). The 2-step
568 approach permits to partially overcome that limitation, with the improvement of the mean seasonal
569 cycle for the three data streams (Figure 2c).

570

571 **3.1.3 Specific improvements at CO₂ stations**

572

573 Figure 3 further analyzes the impact of each assimilation experiment on the fit to the observed
574 atmospheric CO₂ concentrations in terms of the bias in the long-term trend (2000-2009) and fit to the
575 mean seasonal cycle over the same period (i.e., bias in seasonal amplitude and length of the carbon
576 uptake period - CUP - Supplementary text S2). For the trend analysis (Figure 3a), only experiments
577 where atmospheric CO₂ measurements are assimilated are considered.

578 With the default (prior) parameter values, the fluxes simulated by ORCHIDEE and transported by
579 LMD_z overestimate the trend by about 1 ppm.yr⁻¹. When assimilating atmospheric CO₂ data, most of

580 the parameter correction aims at reducing this bias. This is mostly achieved by tuning the regional
581 K_{soilC_reg} parameters: The net land carbon sink is increased globally in order to match the observed
582 trend at most stations (reducing the bias from around 1 ppm.yr⁻¹ to 0.1 ppm.yr⁻¹). Compared to the
583 improvement in the bias in the trend, the improvements (reduction in bias) in the amplitude of the
584 CO₂ seasonal cycle and in the length of the carbon uptake period (CUP) (Figures 3b and c) are
585 marginal. Note that our joint DA experiments lead to lower trend biases compared to the stepwise
586 approach.

587 For the amplitude of CO₂ concentrations, the joint assimilations including CO₂ data lead to lower
588 improvements on average compared to any single data stream assimilation experiment. Interestingly,
589 the highest improvements in CO₂ amplitude are achieved when flux data are assimilated (F or F+VI),
590 which reveals that the constraint on photosynthesis and respiration provided by FLUXNET
591 measurements is consistent with the amplitude of the seasonal atmospheric CO₂ cycle and within the
592 ORCHIDEE-LMDz model (as already pointed out in Kuppel et al. (2014)). Surprisingly, the use of
593 satellite vegetation indices (VI) leads to a slightly lower residual amplitude bias than when
594 atmospheric CO₂ data are assimilated, albeit a lower number of optimized parameters. For the length
595 of the CUP, the relative model correction appears small for almost all experiments and is lower than
596 what is achieved for the trend and amplitude. Some degradation (increased model-data bias) is even
597 obtained for the cases F and F+CO₂. This may be attributed to some inconsistency in the phasing of
598 the CUP derived from the FLUXNET stations and from the atmospheric stations (given differences in
599 the spatial and temporal scale constraints brought each data stream). Among the single data stream
600 assimilations, the highest improvement is obtained for VI where the optimisation of the phenological
601 parameters was the only improvement allowed for tuning the model. For the joint assimilations,
602 those combining the three data streams provide the best performance and perform better than the
603 stepwise approach.

604 Among the joint assimilations with three data streams, the 2-step approach results in the largest
605 reduction in amplitude and CUP bias, but, on the other hand, the larger trend bias.

606

607 **3.2 Impact of the assimilations on regional to global land C fluxes and errors**

608

609 Figure 4 now compares the carbon fluxes (NEE and GPP) at the global scale and for three large
610 regions (northern and southern extra-tropics, and tropics) using hindcast simulations based on the
611 different optimisations.

612 NEE is close to equilibrium by construction in the prior model (about -0.3 GtC.yr⁻¹ globally). Note first
613 that experiments excluding CO₂ data produce land carbon fluxes (from -10 (F+VI) to +6 (VI) GtC.yr⁻¹,

614 not shown in Figure 3) that are not compatible with our understanding of the land C fluxes. For all
615 experiments including atmospheric CO₂ data, the assimilations lead to much more negative NEE
616 (increased land carbon sink) compared to the prior for nearly all regions: the optimized carbon sinks
617 are about -2.4 GtC.yr⁻¹ at the global scale, similar to the stepwise approach (see Supplementary Text
618 S6 for detailed results for each assimilation experiment). Therefore, our joint assimilations with
619 atmospheric CO₂ data result in a land C sink that is in the range of independent TBM estimates of the
620 global net carbon budget (over the same period, the Global Carbon Project reports a global land sink
621 of -2.9 GtC.yr⁻¹ ± 0.8 standard deviation (see Table 5 of Friedlingstein et al., 2020)). Note that we have
622 imposed (see method in §2.1.2) a net emission from land use change (i.e. deforestation) of +1.1
623 GtC.yr⁻¹ (2000-2009) which is slightly lower than that reported in Friedlingstein et al. (2020) from the
624 TBMs (1.6±0.5 GtC.yr⁻¹) or the Bookkeeping methods (1.4±0.7 GtC.yr⁻¹), hence our lower terrestrial
625 carbon sink.

626 These similar posterior global scale budgets however hide large regional contrasts. While the three
627 joint assimilation experiments F+CO₂, VI+CO₂, and F+VI+CO₂, lead to similar NEE budgets across
628 regions (with magnitudes comparable to the stepwise assimilation set-up), the CO₂ and F+VI+CO₂-
629 2steps experiments result in distinctly different estimates. In the northern extra-tropics, the CO₂
630 assimilation results in the largest C sinks (numbers provided in Supplementary Text S6) while the
631 F+VI+CO₂-2steps assimilation leads to the lowest C sink. The reverse is obtained for the Tropics.

632 With a global scale budget of 171 GtC.yr⁻¹ for GPP, the prior ORCHIDEE model is on the high range of
633 recent estimates of the global GPP, as synthesized in Anav et al. (2015), the mean value of which
634 being around 140 GtC.yr⁻¹. Depending on the data assimilated in this study, the posterior GPP ranges
635 from 147 GtC.yr⁻¹ (F+VI) to 170 GtC.yr⁻¹ (VI+CO₂) at the global scale. The largest differences with the
636 prior are obtained for the experiments involving flux and satellite data (alone or the two combined).
637 This is directly linked to large corrections in photosynthesis and phenology parameters for these
638 experiments (see §3.3). In comparison, the assimilations involving atmospheric CO₂ concentrations
639 data are more conservative with respect to GPP. Assimilating atmospheric CO₂ data alone lessens the
640 GPP reduction by a factor of about three compared to assimilations with F and VI data, and the
641 corrections for the joint assimilations using CO₂ data is even lower (cf Supplementary Text S6 for
642 details).

643 By propagating the error on the parameters in the observation space (see Eq. 9), we calculated the
644 uncertainty in NEE and GPP fluxes caused by parameter uncertainty for the prior and optimized
645 models. The error statistics, initially calculated at monthly/grid scale resolutions, were aggregated
646 over the same regions as above, fully accounting for the spatio-temporal correlations between grid
647 cells (Figure 5).

648 At the global scale, the prior error standard deviation for NEE (4.7 GtC.yr^{-1}) is high compared to the
649 typical uncertainty associated to TBMs (about 0.5 GtC.yr^{-1} , Friedlingstein et al. (2020)) or to
650 atmospheric inversions (estimated uncertainty $\sim 0.4 \text{ GtC.yr}^{-1}$ in Peylin et al.(2013)). This is a
651 consequence of neglecting negative error correlations between them (as done in nearly all C cycle DA
652 studies). Given this high prior uncertainty, the posterior error for NEE and GPP are significantly
653 reduced, as expected. Because of the strong dependence of the posterior errors on the optimisation
654 set-up and the fact we do not consider the error of the model, we should only compare the relative
655 error reduction between DA experiments. Noteworthy, the posterior errors in global NEE obtained
656 for the experiments CO₂ and VI+CO₂ are about 15 times lower than the posterior errors resulting
657 from the other data combinations (and three orders of magnitude lower than the prior error). This is
658 due both i) to the need for the DA system to correct the large *a priori* mismatch of the atmospheric
659 CO₂ growth rate and ii) to the lower number of optimized parameters in these configurations (Table
660 2: about 60% more parameters being optimized in F+VI+CO₂ than in CO₂ or VI+CO₂). The joint
661 assimilations result in higher posterior errors on NEE, while they usually lead to the lower posterior
662 errors on GPP. For GPP, the lowest posterior errors are found for the experiments combining F and
663 CO₂ data, while experiments F, CO₂ and VI+CO₂ lead to larger posterior errors. This is due to the fact
664 that i) F and CO₂ data provide a stronger constraint on the annual mean photosynthesis than VI data
665 and that ii) F and CO₂ data provide cross constraints on photosynthesis. Experiment VI, in which
666 about ten times fewer parameters are optimized and targeting primarily the timing of phenology,
667 results in the highest posterior GPP errors (although still a reduction from the prior).
668 Finally, one can observe that the posterior errors are higher in the tropics for both NEE and GPP (and
669 the reduction compared to the prior error is lower), which is even more prominent in the
670 experiments using *in situ* flux data alone or with satellite data, a direct consequence of the lower
671 data availability (eddy-covariance measurements) to constrain the model parameters for tropical
672 PFTs.

673

674 **3.3 Parameter estimates and associated uncertainties**

675

676 Figure 6 shows the impacts of the different assimilation experiments on a subset of the retrieved
677 parameter values and their associated uncertainties (the remaining parameters are shown in Figure
678 S2).

679 While the stepwise study showed only few changes in the parameter estimates between the
680 sequential steps (and hence as a function of the data stream from which the parameters were
681 constrained) (Peylin et al., 2016), our results show a large variability between the assimilation

682 experiments. For most parameters, the highest departures from the prior values are obtained for the
683 single-data stream assimilations. Higher changes are obtained for flux or satellite data as compared
684 to the estimates retrieved with atmospheric CO₂ data alone which remain closer to the prior values.
685 This reflects the lower constraint brought by the CO₂ assimilation experiment on photosynthesis and
686 phenology related processes, as already pointed out in §3.1.2. This is largely due to the correction of
687 the trend bias via a few respiration related parameters, which prevails over the improvement of the
688 other photosynthesis and phenology parameters.

689 The joint assimilations usually result in a lower departure from the background. For the parameters
690 constrained by two data streams, the optimized values generally fall in between those retrieved
691 when these data streams are assimilated alone. This feature shows how the system tries to find a
692 compromise solution and illustrates potential overfitting with only one data stream. The values
693 optimized in the three experiments involving atmospheric CO₂ data show little variability for all
694 parameters, except in F+VI+CO₂-2steps where the tuning of the multiplicative parameter of regional
695 soil carbon pools $K_{soilC_{reg}}$ is decoupled from the optimization of the other photosynthesis and
696 phenological parameters. The decrease of $K_{soilC_{reg}}$ parameters from the prior value is very small in all
697 experiments, although these parameters are responsible for most of the correction of the
698 atmospheric CO₂ trend. This highlights the challenge of optimizing soil C disequilibrium with our
699 approach based on a model spin-up followed by only a short transient period. The smallest $K_{soilC_{reg}}$
700 changes are obtained for the 2-step approach. Note that in this approach, $Q10$ is also estimated in
701 the first step; the corresponding estimate is similar to the value retrieved in the second step (which is
702 displayed in Figure 3), below 0.5% difference, and consistent with the estimates of the other joint
703 assimilation experiments. For some parameters/PFTs, the direction of the departure with respect to
704 the prior value (increase or decrease) may differ depending on the data stream assimilated (as
705 detailed in S5).

706 At the first order, the estimated parameter uncertainties decrease with the number of observations
707 assimilated, as expected from Equation 4, and given that the observations are treated as
708 independent data. However, given that the estimated parameter errors strongly depend on the set-
709 up of **B** and **R** matrices and that we did not use error correlations in these matrices, we should only
710 focus on the relative error reduction between experiments. The uncertainty reduction achieved
711 through the assimilation of atmospheric CO₂ data is usually lower than when flux and satellite data
712 are assimilated alone, and typically vary between 10% and 60% for most photosynthetic and
713 phenological parameters. Most often, the joint assimilations involving two data streams result in an
714 uncertainty reduction higher or of the same order than that achieved in the single-data assimilations.
715 The joint assimilation combining the three data streams generally results in the highest uncertainty
716 reduction, with values typically between 60% and 90%. The values are much higher than those

717 inferred from the stepwise approach, which are more on the order of the uncertainty reduction
718 obtained in the CO₂ assimilation experiment.

719

720 **3.4 Relative constraints brought by the different datasets**

721

722 We now quantify the impact of each of the three data streams on the analysis using the global
723 average observation influence (quantified by OI) and information content (DFS) metrics defined in
724 §2.4.4. We recall that OI (i.e. trace of \mathbf{S} normalized by the number of observations) gauges the
725 average influence that each single observation has on the analysis, while the relative DFS measures
726 the overall weight of one data stream in the optimization (the difference between OI and DFS is due
727 to the number of observations assimilated, Cardinali et al. (2014)). OI and DFS are determined for the
728 joint assimilation experiments combining the three data streams.

729 Because of the very large number of observations (above 300,000) involved in the assimilation, only
730 the diagonal elements of the influence matrix (Eq. 10) can be calculated. The trace of \mathbf{S} measures the
731 equivalent number of parameters and is equal to 132. Such a value, lower than the number of
732 parameters (182), indicates that the optimized parameters may not be fully independent (although
733 parameter error correlations have been ignored in our \mathbf{B} matrix) as already reported in Kuppel et al.
734 (2012), or that some are not constrained during the optimisation process (as for instance LAI_{MAX}
735 which estimates remains at its *a priori* value for some PFTs, Figure S2).

736 The values of OI are provided in Table 4 for flux, NDVI and atmospheric CO₂ data. With about the
737 same number of observations considered (Table 2, last column), one *in situ*_flux measurement has
738 about 10 times more weight than one NDVI observation. This is a consequence of the larger number
739 of parameters constrained by flux measurements than by NDVI data in our set-up. The highest
740 influence is found for atmospheric CO₂ data, the relative weight of one atmospheric CO₂
741 measurement being 4 times larger than that of one flux observation, albeit the much lower number
742 of data assimilated. Again, this is a consequence of the strong weight of the mismatch between the *a*
743 *priori* simulated and the observed atmospheric CO₂ trend, which is drastically reduced through the
744 optimisation.

745 However, the smaller number of atmospheric CO₂ data assimilated, compared to flux and NDVI
746 datasets, reduces the overall constraint on the analysis provided by atmospheric CO₂ data, as gauged
747 by its relative DFS. Hence, our optimization is mainly controlled by flux data which have an overall
748 contribution of about 75%, that is about 5 times larger than the constraint brought by atmospheric
749 CO₂ data and 7 times larger than that of satellite NDVI. Differences between F+VI+CO₂ and
750 F+VI+CO₂-2steps are relatively small for both OI and DFS but show a slightly lower weight of

751 atmospheric CO₂ data for the 2 steps experiment. A complementary analysis in which the influence
752 of each PFT and each atmospheric station is differentiated is provided in Supplementary Text S7.

753

754 **4 Discussion**

755

756 **4.1 Benefits of simultaneous assimilations**

757 Joint/simultaneous assimilations are more complex to implement compared to stepwise/sequential
758 assimilations. In principle a stepwise approach could lead to similar results than a simultaneous
759 approach, if the posterior parameter error covariance matrix could be fully characterized at each
760 assimilation step and further propagated as prior information in the next step. However, given that
761 this is difficult in practice, and because of model non-linearities and equifinal solutions,
762 stepwise/joint approaches lead to different optimized models (Kaminski et al., 2012; MacBean et al.
763 2016). With a joint assimilation, biases and incompatibilities between data streams may impact more
764 directly a larger set of parameters than in a stepwise assimilation. The characterization of the prior
765 observation errors also becomes more critical as they condition the relative weight of the
766 observations in the misfit function to minimize and their influence on the solution (analysis). Here,
767 we designed several tests beforehand to refine the configuration of the framework for the
768 simultaneous assimilations. Relying on consistency metrics of Desroziers et al. (2005), we improved
769 the prior error statistics on the model parameters and checked that they were consistent with both
770 the prior model-data mismatch and the observations errors for the different data streams. In spite of
771 the limitation of their application to non-linear models like ORCHIDEE, their implementation has
772 proved to be useful and has led to an improved consistency of the optimized models at regional and
773 global scales.

774 Single data stream assimilations usually lead to the best model - data fit for the assimilated data
775 stream, as compared to joint assimilations. However, most often these single data stream
776 assimilations also produce degraded results with respect to the data that were not assimilated. This
777 reveals potential overfitting issues with a higher variability of the optimized parameter values than in
778 the joint assimilations. Overfitting is a key issue for DA studies which can be partly alleviated when
779 combining different data streams within a consistent framework: Because they bring different
780 information on the model processes, they contribute to better circumscribing a set of model
781 parameters. Among the several assimilation experiments considered, those where several data were
782 assimilated simultaneously were those in which there was always an improvement in optimized

783 variables (i.e. no deterioration in model-data fit). The joint assimilations resulted in a reduced
784 variability in parameter estimates and in optimized NEE and GPP.

785

786 **4.2 Realism of the regional to global-scale C fluxes**

787 The overarching objective of the study was more about assessing how to make the best of a
788 synergistic exploitation of different data streams within a consistent assimilation framework rather
789 than achieving an up-to-date re-analysis of the global carbon fluxes. Especially since we focused on a
790 limited dataset both in terms of temporal coverage (no atmospheric CO₂ data nor satellite data after
791 2010, no *in situ* flux data beyond 2007) and of informational constraint. Indeed, we did not assess the
792 potential of other data that can bring relevant (and possibly more direct) additional constraints on
793 the dynamics of terrestrial carbon stocks and fluxes, such as aboveground biomass (Thum et al., 2017)
794 or Solar Induced-Fluorescence (Bacour et al., 2019) which have already been investigated with
795 ORCHIDAS, and with an updated version of the ORCHIDEE model. The expansion of the assimilated
796 datasets to provide the most up-to-date constraint on modeled carbon fluxes will be the subject of
797 future work.

798 In spite of these limitations, we saw that the regional/global estimated NEE and GPP budgets are
799 realistic and in agreement with independent estimates. There are still important differences in the
800 model predictions for the different assimilation experiments (and we have not attempted to identify
801 what was the most reliable optimized model, which would require the use of an ensemble of
802 independent data, an effort beyond the scope of this paper). Still, our optimised simulations allow a
803 more in depth exploration of the partitioning of the land carbon budget between the northern extra-
804 tropics and the tropics. From the global carbon budget, a discrepancy exists between the partition
805 estimated by the atmospheric CO₂ inversions and by the terrestrial biosphere models (Kondo et al.,
806 2020). Atmospheric inversions estimate a larger sink over the northern extra-tropics than TBMs
807 (around 1.8 GtC.yr⁻¹ versus 1.0 GtC.yr⁻¹ for the period 2010-2020), although with large variations
808 between TBMs (Friedlingstein et al., 2020, Figure 8). Conversely, TBMs estimate a larger C sink over
809 the tropics (Ahlström et al., 2015; Sitch et al., 2015), possibly due to strong CO₂ fertilization effects in
810 TBMs (Schimel et al., 2015), than the inversions, which estimate an approximately net neutral C sink
811 (Peiro et al., 2022). The F+VI+CO₂-2steps assimilation follows the typical partitioning pattern of
812 TBMs' behavior, with a stronger C sink in the tropics than in the northern hemisphere (Figure 4). In
813 contrast, all other multiple data stream experiments with CO₂ included (F+CO₂, VI+CO₂ and
814 F+VI+CO₂) and the stepwise lead to an approximately equal C sink in the northern hemisphere and
815 tropics (thus unlike the general pattern for TBMs, and more in line with atmospheric inversions); And
816 on the other hand, the CO₂ experiment leads to a similar regional partitioning as the atmospheric

817 inversions. For the F+VI+CO₂-2steps experiment, the tropical sink is almost doubled as compared to
818 the other simultaneous assimilation experiments in spite of a slightly reduced GPP.

819

820 **4.3 Caveats and perspectives concerning the initialisation of the soil carbon pools**

821 We showed that reaching the global terrestrial carbon sink was mostly achieved by correcting the
822 initial soil carbon reservoirs in the ORCHIDEE model. Their tuning enables the correction of the
823 biased trend between atmospheric CO₂ time series measurements at stations and the prior
824 ORCHIDEE-LMDz model. The impact of this biased trend on the optimization performance was
825 highlighted by the quantification of the influence for the three data streams on the optimization,
826 with atmospheric CO₂ data having the largest average observation influence on the solution. A
827 consequence of correcting the biased trend is that the model improvement with respect to other
828 processes (photosynthesis, phenology) is hindered.

829 From a more general perspective, the detrimental consequences of model-data biases become even
830 more important when assimilating multiple observational constraints because of their
831 interconnected contribution to the model calibration. It should be noted that the impact of
832 systematic model-data errors is not inherent to our minimization approach (gradient-based) and has
833 also been highlighted using random search approaches (Brynjarsdóttir and O'Hagan, 2014; Cameron
834 et al., 2022). Thus, accounting for bias correction approaches into data assimilation schemes (Dee,
835 2005; Trémolet, 2006; Kumar et al., 2012) becomes increasingly important as the complexity of
836 models and the number of observational constraints increase.

837 We attempted here to overcome this by setting up a 2-step assimilation process where the trend
838 correction is mostly achieved in the first step by tuning the regional parameters controlling the soil
839 carbon pools. In doing so, the 2-step approach optimizes the constraint brought by *in situ* and
840 satellite data (in the second step) in the joint assimilation process. Therefore, the 2-step results in
841 enhanced model-data consistencies compared to a standard simultaneous assimilation (as observed
842 in Figure 2 and Figure 3) with a caveat regarding atmospheric CO₂ data (the improved fit is mostly
843 with the detrended atmospheric CO₂ data but not the raw data) and the distribution of the land C
844 sink (we saw above that this experiment tends to favor a tropical C sink). We acknowledge the fact
845 that this way of doing is not optimal and requires further investigation. Going beyond the steady
846 state assumption following model spin-up has been discussed already (Carvalhais et al., (2010);
847 MacBean et al., 2022), as steady state results in biased estimates of soil carbon reservoirs (Exbrayat
848 et al., 2014). Extending the period for the transient simulations following spin-up, like it is done in the
849 TRENDY experiment (Sitch et al., 2015), would have led to more realistic soil C imbalance and
850 increased the consistency of the modelled atmospheric data with the measurements. Improving the

851 representation of soil carbon stock trajectories in TBMs is pivotal to predicting NEE in regional to
852 global assessments of the capacity of the terrestrial ecosystems to absorb or not atmospheric CO₂.
853 We used here atmospheric CO₂ data to optimize a scalar that accounts for the soil C disequilibrium.
854 The optimization of scaling factors of soil carbon pools is a handy alternative to the optimization of
855 the parameters controlling the turnover times and soil carbon input of the ORCHIDEE soil C model.
856 This would require that the spin-up (over at least one thousand years) and transient simulations are
857 included in the minimization process at each iteration; the prohibitive calculation times for
858 performing this type of optimisation precludes us doing this for now. Exploiting in TBMs databases
859 more directly related to regional soil carbon contents (such as the Harmonized World Soil Database
860 (HWSD) (FAO/IIASA/ISRIC/ISSCAS/JRC, 2012), the International Soil Carbon Network, Nave et al.
861 (2016), or the global soil respiration database, Jian et al. (2021)) is not straightforward because of the
862 errors associated with these datasets (Todd-Brown et al., 2013), and inconsistencies between the
863 estimated quantities and the model state variables and underlying processes (as for instance the
864 depth of the soil carbon). In any case, what is sorely needed is data that track changes in C stocks
865 over long time periods. Still, it is of primary importance for the science community to endeavor to
866 bridge the gap between state-of-the-art estimates of soil carbon stocks and the quantities that TBMs
867 simulate over the historical period.

868

869 **5 Conclusion**

870 By assimilating simultaneously or separately up to three independent carbon-cycle related data
871 streams (*in situ* measurements of net carbon and latent heat fluxes, satellite derived NDVI data, and
872 measurements of atmospheric CO₂ concentration at surface stations) within the ORCHIDEE global
873 model (and an offline transport model based on pre-calculated transport fields with LMDz), we have
874 been able to analyze their compatibility, complementarity, and usefulness, in the frame of a global-
875 scale carbon data assimilation system. To do so, the study relied on different metrics to set-up and
876 interpret the assimilation performances. The approach as well as the explored metrics are general
877 enough to benefit to a broader set of data assimilation applications, supporting guidance for setting
878 up such a C cycle DA framework and for better use of the data to be assimilated.

879 We investigated how the different combinations of data streams constrain the parameters of the
880 ORCHIDEE land surface model, and by consequence the simulated historical spatial and temporal
881 distribution of the net and gross carbon fluxes (NEE and GPP), as well as FAPAR and atmospheric CO₂
882 concentrations. We quantified how the combination of these data-streams (two by two or
883 altogether) impacts the reliability of the model predictions. Although it leads to lower fitting
884 performances with respect to the assimilation of any individual dataset (because the optimization

885 seeks for a trade-off solution between all data-streams) the simultaneous assimilation of the three
886 data-streams is found to be the most consistent approach. In particular, it avoids model overfitting
887 which can degrade the model predictions with respect to data-streams not assimilated. The
888 successive model evaluations performed after the assimilation highlighted challenges in handling
889 model-data bias in Bayesian optimisation frameworks.

890 In this study, we focused on biases associated to the initialisation of the soil carbon pools in our set-
891 up (the fact that they are out of equilibrium because of all historical land cover change and land
892 management impacts). A careful spin-up including a transient simulation to account for the impact of
893 all past disturbances (climate, land cover, land management) is mandatory but likely not sufficient
894 (due to uncertainties in the historical evolution of these drivers) to achieve accurate simulation of
895 the space-time distribution of the global land C sink. Next steps should focus on including part of the
896 spin-up (i.e. such as the transient simulation) in the assimilation procedure possibly in conjunction
897 with initial C pool optimisation.

898 Terrestrial ecosystem modelers are anticipating the many novel types of observations that are being
899 made available for model evaluation and assimilation. As a result, and in parallel to the growing
900 complexity of TBMs incorporating new biogeo- physical processes related to the carbon and water
901 cycles, new observation operators are being developed to be able to make use of this new wealth of
902 data. With these new perspectives ahead, the global land surface modeling community should
903 investigate more deeply some of the issues highlighted in this study and linked to multiple data
904 streams assimilation, initial model state optimisation and/or the inclusion of the spin up in the DA
905 system, etc., in order to achieve significant reduction in land surface model projection uncertainties.

906
907

908 **Code availability**

909 The ORCHIDEE model code is open source (<http://forge.ipsl.jussieu.fr/orchidee>) and the associated
910 documentation can be found at <https://forge.ipsl.jussieu.fr/orchidee/wiki/Documentation>. The
911 ORCHIDAS data assimilation scheme (in Python) is available through a dedicated web site
912 (<https://orchidas.lsce.ipsl.fr/>). Information about the LMDz model, source code and contact is
913 provided at <https://lmdz.lmd.jussieu.fr/le-projet-lmdz-en-bref-en>.

914

915 **Data availability**

916 This work used eddy covariance data acquired by the FLUXNET community
917 (<https://fluxnet.org/data/la-thuille-dataset/>). The NDVI data are derived from the MODIS
918 MOD09CMG collection 5 daily global reflectance products

919 (<https://ladsweb.modaps.eosdis.nasa.gov/missions-and-measurements/products/MOD09CMG>). The
920 surface atmospheric CO₂ concentration data uses measurements from The NOAA Earth System
921 Laboratory (ESRL) archive (<ftp://ftp.cmdl.noaa.gov/ccg/co2/>), the CarboEurope IP project
922 (http://ceatmosphere.lsce.ipsl.fr/database/index_database.html), and the World Data Centre for
923 Greenhouse Gases of the World Meteorological Organization Global Atmospheric Watch Programme
924 (<http://gaw.kishou.go.jp>).

925

926 **Author contributions**

927 CB, NM, PP and FC conceived the research. CB developed the data assimilation system with
928 contribution from FC (coupling with LMDz) and SL (parallelisation and post-processing). PP developed
929 the offline transport (precomputed Jacobian matrix of LMDz) with contribution from SL. CB
930 conducted the analysis, with contributions from NM and SL for spin-up ORCHIDEE simulations. PP, FC,
931 and EK, provided the ancillary input fluxes for the global-scale simulations. EK and CB contributed to
932 the development of the tangent linear version of the ORCHIDEE model. CB conceived and wrote the
933 original draft with NM, PP, and FC. All co-authors reviewed the paper.

934

935

936 **Acknowledgements**

937 This work has been supported by the CARBONES project, within the EU's 7th Framework Program for
938 Research and Development. The authors are very grateful to LSCE's IT staff for their support and for
939 the computing resources, as well as to the ORCHIDEE Project Team for developing and maintaining
940 the ORCHIDEE code.

941

942 **References**

943 Ahlström, A., Raupach, M. R., Schurgers, G., Smith, B., Arneth, A., Jung, M., Reichstein, M., Canadell, J.
944 G., Friedlingstein, P., and Jain, A. K.: The dominant role of semi-arid ecosystems in the trend and
945 variability of the land CO₂ sink, *Science*, 48(6237), 895–899, 2015.

946 Anderson, J., Hoar, T., Raeder, K., Liu, H., Collins, N., Torn, R., & Avellano, A. (2009). The data
947 assimilation research testbed: A community facility. *Bulletin of the American Meteorological Society*,
948 90(9), 1283-1296.

949 Arora, V. K., Katavouta, A., Williams, R. G., Jones, C. D., Brovkin, V., Friedlingstein, P., Schwinger, J.,
950 Bopp, L., Boucher, O., and Cadule, P.: Carbon–concentration and carbon–climate feedbacks in CMIP6
951 models and their comparison to CMIP5 models, *Biogeosciences*, 17(16), 4173–4222, 2020.

952 Bacour, C., Peylin, P., MacBean, N., Rayner, P. J., Delage, F., Chevallier, F., Weiss, M., Demarty, J.,
953 Santaren, D., and Baret, F.: Joint assimilation of eddy covariance flux measurements and FAPAR
954 products over temperate forests within a process-oriented biosphere model, *Journal of Geophysical
955 Research: Biogeosciences*, 120(9), 1839–1857, 2015.

956 Bacour, C., Maignan, F., Peylin, P., Macbean, N., Bastrikov, V., Joiner, J., Köhler, P., Guanter, L., and
957 Frankenberg, C.: Differences between OCO-2 and GOME-2 SIF products from a model-data fusion
958 perspective, *Journal of Geophysical Research: Biogeosciences*, 124(10), 3143–3157, 2019.

959 Bastrikov, V., MacBean, N., Bacour, C., Santaren, D., Kuppel, S., and Peylin, P.: Land surface model
960 parameter optimisation using in situ flux data: comparison of gradient-based versus random search
961 algorithms (a case study using ORCHIDEE v1. 9.5. 2), *Geoscientific Model Development*, 11(12),
962 4739–4754, 2018.

963 Botta, A., Viovy, N., Ciais, P., Friedlingstein, P., and Monfray, P.: A global prognostic scheme of leaf
964 onset using satellite data, *Global Change Biology*, 6(7), 709–725, 2000.

965 Brynjarsdóttir, J., & O’Hagan, A.: Learning about physical parameters: The importance of model
966 discrepancy, *Inverse problems*, 30(11), 114007, 2014.

967 Byrd, R. H., Lu, P., Nocedal, J., and Zhu, C.: A limited memory algorithm for bound constrained
968 optimization, *SIAM Journal on scientific computing*, 16(5), 1190–1208, 1995.

969 Cameron, D., Hartig, F., Minunno, F., Oberpriller, J., Reineking, B., Van Oijen, M., & Dietze, M.: Issues
970 in calibrating models with multiple unbalanced constraints: the significance of systematic model and
971 data errors, *Methods in Ecology and Evolution*, 13(12), 2757–2770, 2022.

972 Cardinali, C., Pezzulli, S., and Andersson, E.: Influence-matrix diagnostic of a data assimilation system,
973 *Quarterly Journal of the Royal Meteorological Society: A journal of the atmospheric sciences, applied
974 meteorology and physical oceanography*, 130(603), 2767–2786, 2004.

975 Carvalhais, N., Reichstein, M., Ciais, P., Collatz, G. J., Mahecha, M. D., Montagnani, L., Papale, D.,
976 Rambal, S., and Seixas, J.: Identification of vegetation and soil carbon pools out of equilibrium in a
977 process model via eddy covariance and biometric constraints, *Global Change Biology*, 16(10), 2813–
978 2829, 2010.

979 Chevallier, F., Bréon, F. M., & Rayner, P. J.: Contribution of the Orbiting Carbon Observatory to the
980 estimation of CO₂ sources and sinks: Theoretical study in a variational data assimilation framework,
981 *Journal of Geophysical Research: Atmospheres*, 112(D9), 2007.

982 Cressot, C., Chevallier, F., Bousquet, P., Crevoisier, C., Dlugokencky, E. J., Fortems-Cheiney, A.,
983 Frankenberg, C., Parker, R., Pison, I., and Scheepmaker, R. A.: On the consistency between global and
984 regional methane emissions inferred from SCIAMACHY, TANSO-FTS, IASI and surface measurements,
985 *Atmospheric Chemistry and Physics*, 14(2), 577–592, 2014.

986 Crowell, S., Baker, D., Schuh, A., Basu, S., Jacobson, A. R., Chevallier, F., Liu, J., Deng, F., Feng, L., and
987 McKain, K.: The 2015–2016 carbon cycle as seen from OCO-2 and the global in situ network,
988 *Atmospheric Chemistry and Physics*, 19(15), 9797–9831, 2019.

989 Dee, D. P.: Bias and data assimilation, *Quarterly Journal of the Royal Meteorological Society: A*
990 *journal of the atmospheric sciences, applied meteorology and physical oceanography*, 131(613),
991 3323–3343, 2005.

992 Dee, D. P., Uppala, S. M., Simmons, A. J., Berrisford, P., Poli, P., Kobayashi, S., Andrae, U., Balmaseda,
993 M. A., Balsamo, G., and Bauer, d P.: The ERA-Interim reanalysis: Configuration and performance of
994 the data assimilation system, *Quarterly Journal of the royal meteorological society*, 137(656), 553–
995 597, 2011.

996 Desroziers, G., Berre, L., Chapnik, B., and Poli, P.: Diagnosis of observation, background and analysis-
997 error statistics in observation space, *Quarterly Journal of the Royal Meteorological Society: A journal*
998 *of the atmospheric sciences, applied meteorology and physical oceanography*, 131(613), 3385–3396,
999 2005.

1000 Dietze, M. C., Lebauer, D. S., and Kooper, R. O. B.: On improving the communication between models
1001 and data, *Plant, Cell & Environment*, 36(9), 1575-1585, 2013.

1002 Dufresne, J.-L., Foujols, M.-A., Denvil, S., Caubel, A., Marti, O., Aumont, O., Balkanski, Y., Bekki, S.,
1003 Bellenger, H., and Benschila, R.: Climate change projections using the IPSL-CM5 Earth System Model:
1004 from CMIP3 to CMIP5, *Climate dynamics*, 40(9), 2123–2165, 2013.

1005 Exbrayat, J.-F., Pitman, A. J., and Abramowitz, G.: Response of microbial decomposition to spin-up
1006 explains CMIP5 soil carbon range until 2100, *Geoscientific Model Development*, 7(6), 2683–2692,
1007 2014.

1008 Forkel, M., Carvalhais, N., Schaphoff, S., Migliavacca, M., Thurner, M., and Thonicke, K.: Identifying
1009 environmental controls on vegetation greenness phenology through model–data integration,
1010 *Biogeosciences*, 11(23), 7025–7050, 2014.

1011 Fox, A. M., Hoar, T. J., Anderson, J. L., Arellano, A. F., Smith, W. K., Litvak, M. E., MacBean, N., Schimel,
1012 D. S., and Moore, D. J.: Evaluation of a data assimilation system for land surface models using CLM4.
1013 5, *Journal of Advances in Modeling Earth Systems*, 10(10), 2471–2494, 2018.

1014 Friedlingstein, P., O’Sullivan, M., Jones, M. W., Andrew, R. M., Hauck, J., Olsen, A., Peters, G. P.,
1015 Peters, W., Pongratz, J., Sitch, S., Le Quéré, C., Canadell, J. G., Ciais, P., Jackson, R. B., Alin, S., Aragão,
1016 L. E. O. C., Arneeth, A., Arora, V., Bates, N. R., Becker, M., Benoit-Cattin, A., Bittig, H. C., Bopp, L.,
1017 Bultan, S., Chandra, N., Chevallier, F., Chini, L. P., Evans, W., Florentie, L., Forster, P. M., Gasser, T.,
1018 Gehlen, M., Gilfillan, D., Gkritzalis, T., Gregor, L., Gruber, N., Harris, I., Hartung, K., Haverd, V.,
1019 Houghton, R. A., Ilyina, T., Jain, A. K., Joetzjer, E., Kadono, K., Kato, E., Kitidis, V., Korsbakken, J. I.,
1020 Landschützer, P., Lefèvre, N., Lenton, A., Lienert, S., Liu, Z., Lombardozzi, D., Marland, G., Metzl, N.,
1021 Munro, D. R., Nabel, J. E. M. S., Nakaoka, S.-I., Niwa, Y., O’Brien, K., Ono, T., Palmer, P. I., Pierrot, D.,
1022 Poulter, B., Resplandy, L., Robertson, E., Rödenbeck, C., Schwinger, J., Séférian, R., Skjelvan, I., Smith,
1023 A. J. P., Sutton, A. J., Tanhua, T., Tans, P. P., Tian, H., Tilbrook, B., van der Werf, G., Vuichard, N.,
1024 Walker, A. P., Wanninkhof, R., Watson, A. J., Willis, D., Wiltshire, A. J., Yuan, W., Yue, X., and Zaehle,
1025 S.: Global Carbon Budget 2020, *Earth System Science Data*, 12(4), 3269–3340, 2020.

1026 Giering, R., Kaminski, T., and Slawig, T.: Generating efficient derivative code with TAF: Adjoint and
1027 tangent linear Euler flow around an airfoil, *Future generation computer systems*, 21(8), 1345–1355,
1028 2005.

1029 Groenendijk, M., Dolman, A. J., Van Der Molen, M. K., Leuning, R., Arneeth, A., Delpierre, N., Gash, J. H.
1030 C., Lindroth, A., Richardson, A. D., and Verbeeck, H.: Assessing parameter variability in a
1031 photosynthesis model within and between plant functional types using global Fluxnet eddy
1032 covariance data, *Agricultural and forest meteorology*, 151(1), 22–38, 2011.

1033 Hourdin, F., Musat, I., Bony, S., Braconnot, P., Codron, F., Dufresne, J.-L., Fairhead, L., Filiberti, M.-A.,
1034 Friedlingstein, P., and Grandpeix, J.-Y.: The LMDZ4 general circulation model: climate performance
1035 and sensitivity to parametrized physics with emphasis on tropical convection, *Climate Dynamics*,
1036 27(7), 787–813, 2006.

1037 Jian, J., Vargas, R., Anderson-Teixeira, K., Stell, E., Herrmann, V., Horn, M., Kholod, N., Manzon, J.,
1038 Marchesi, R., and Paredes, D.: A restructured and updated global soil respiration database (SRDB-V5),
1039 Earth System Science Data, 13(2), 255–267, 2021.

1040 Kaminski, T., Knorr, W., Rayner, P. J., and Heimann, M.: Assimilating atmospheric data into a
1041 terrestrial biosphere model: A case study of the seasonal cycle, Global Biogeochemical Cycles, 16(4),
1042 14–1, 2002.

1043 Kaminski, T., Knorr, W., Schürmann, G., Scholze, M., Rayner, P. J., Zaehle, S., Blessing, S., Dorigo, W.,
1044 Gayler, V., and Giering, R.: The BETHY/JSBACH carbon cycle data assimilation system: Experiences
1045 and challenges, Journal of Geophysical Research: Biogeosciences, 118(4), 1414–1426, 2013.

1046 Kato, T., Knorr, W., Scholze, M., Veenendaal, E., Kaminski, T., Kattge, J., and Gobron, N.:
1047 Simultaneous assimilation of satellite and eddy covariance data for improving terrestrial water and
1048 carbon simulations at a semi-arid woodland site in Botswana, Biogeosciences, 10(2), 789–802, 2013.

1049 Keenan, T. F., Davidson, E. A., Munger, J. W., and Richardson, A. D.: Rate my data: quantifying the
1050 value of ecological data for the development of models of the terrestrial carbon cycle, Ecological
1051 Applications, 23(1), 273–286, 2013.

1052 Klonecki, A., Pommier, M., Clerbaux, C., Ancellet, G., Cammas, J. P., Coheur, P. F., ... & Turquety, S.:
1053 Assimilation of IASI satellite CO fields into a global chemistry transport model for validation against
1054 aircraft measurements. Atmospheric Chemistry and Physics, 12(10), 4493-4512, 2012.

1055 Knorr, W. and Heimann, M.: Impact of drought stress and other factors on seasonal land biosphere
1056 CO₂ exchange studied through an atmospheric tracer transport model, Tellus B, 47(4), 471–489,
1057 1995.

1058 Knorr, W. and Kattge, J.: Inversion of terrestrial ecosystem model parameter values against eddy
1059 covariance measurements by Monte Carlo sampling, Global change biology, 11(8), 1333–1351, 2005.

1060 Knorr, W., Kaminski, T., Scholze, M., Gobron, N., Pinty, B., Giering, R., and Mathieu, P.-P.: Carbon
1061 cycle data assimilation with a generic phenology model, Journal of Geophysical Research:
1062 Biogeosciences, 115(G4), 2010.

1063 Kondo, M., Patra, P. K., Sitch, S., Friedlingstein, P., Poulter, B., Chevallier, F.,... & Ziehn, T.: State of the
1064 science in reconciling top-down and bottom-up approaches for terrestrial CO₂ budget, Global change
1065 biology, 26(3), 1068-1084, 2020.

1066 Koffi, E. N., Rayner, P. J., Scholze, M., and Beer, C.: Atmospheric constraints on gross primary
1067 productivity and net ecosystem productivity: Results from a carbon-cycle data assimilation system,
1068 *Global Biogeochemical Cycles*, 26(1), 2012.

1069 Krinner, G., Viovy, N., de Noblet-Ducoudré, N., Ogée, J., Polcher, J., Friedlingstein, P., Ciais, P., Sitch,
1070 S., and Prentice, I. C.: A dynamic global vegetation model for studies of the coupled atmosphere-
1071 biosphere system, *Global Biogeochemical Cycles*, 19(1), 2005.

1072 Kumar, S. V., Reichle, R. H., Harrison, K. W., Peters-Lidard, C. D., Yatheendradas, S., & Santanello, J. A.:
1073 A comparison of methods for a priori bias correction in soil moisture data assimilation, *Water*
1074 *Resources Research*, 48(3), 2012.

1075 Kuppel, S., Peylin, P., Chevallier, F., Bacour, C., Maignan, F., and Richardson, A. D.: Constraining a
1076 global ecosystem model with multi-site eddy-covariance data, *Biogeosciences*, 9(10), 3757–3776,
1077 2012.

1078 Kuppel, S., Chevallier, F., and Peylin, P.: Quantifying the model structural error in carbon cycle data
1079 assimilation systems, *Geoscientific Model Development*, 6(1), 45–55, 2013.

1080 Kuppel, S., Peylin, P., Maignan, F., Chevallier, F., Kiely, G., Montagnani, L., and Cescatti, A.: Model-
1081 data fusion across ecosystems: from multisite optimizations to global simulations, *Geoscientific*
1082 *Model Development*, 7(6), 2581–2597, 2014.

1083 Luo, Y. Q., Randerson, J. T., Abramowitz, G., Bacour, C., Blyth, E., Carvalhais, N., Ciais, P., Dalmonech,
1084 D., Fisher, J. B., Fisher, R., Friedlingstein, P., Hibbard, K., Hoffman, F., Huntzinger, D., Jones, C. D.,
1085 Koven, C., Lawrence, D., Li, D. J., Mahecha, M., Niu, S. L., Norby, R., Piao, S. L., Qi, X., Peylin, P.,
1086 Prentice, I. C., Riley, W., Reichstein, M., Schwalm, C., Wang, Y. P., Xia, J. Y., Zaehle, S., and Zhou, X. H.:
1087 A framework for benchmarking land models, *Biogeosciences*, 9(10), 3857–3874, 2012.

1088 MacBean, N., Maignan, F., Peylin, P., Bacour, C., Bréon, F.-M., and Ciais, P.: Using satellite data to
1089 improve the leaf phenology of a global terrestrial biosphere model, *Biogeosciences*, 12(23), 7185–
1090 7208, 2015.

1091 MacBean, N., Peylin, P., Chevallier, F., Scholze, M., and Schürmann, G.: Consistent assimilation of
1092 multiple data streams in a carbon cycle data assimilation system, *Geoscientific Model Development*,
1093 9(10), 3569–3588, 2016.

1094 MacBean, N., Bacour, C., Raoult, N., Bastrikov, V., Koffi, E. N., Kuppel, S., Maignan, F., Ottlé, C.,
1095 Peaucelle, M., Santaren, D., and Peylin, P.: Quantifying and Reducing Uncertainty in Global Carbon

1096 Cycle Predictions: Lessons and Perspectives From 15 Years of Data Assimilation Studies with the
1097 ORCHIDEE Terrestrial Biosphere Model, *Global Biogeochemical Cycles*, e2021GB007177, 2022.

1098 Migliavacca, M., Meroni, M., Busetto, L., Colombo, R., Zenone, T., Matteucci, G., Manca, G., and
1099 Seufert, G.: Modeling gross primary production of agro-forestry ecosystems by assimilation of
1100 satellite-derived information in a process-based model, *Sensors*, 9(02), 922–942, 2009.

1101 Moore, D. J., Hu, J., Sacks, W. J., Schimel, D. S., and Monson, R. K.: Estimating transpiration and the
1102 sensitivity of carbon uptake to water availability in a subalpine forest using a simple ecosystem
1103 process model informed by measured net CO₂ and H₂O fluxes, *Agricultural and Forest Meteorology*,
1104 148(10), 1467–1477, 2008.

1105 Nave, L., Johnson, K., van Ingen, C., Agarwal, D., Humphrey, M., and Beekwilder, N.: International Soil
1106 Carbon Network (ISCN) Database v3-1, International Soil Carbon Network (ISCN), 2016.

1107 Oberpriller, J., Cameron, D. R., Dietze, M. C., & Hartig, F.: Towards robust statistical inference for
1108 complex computer models. *Ecology Letters*, 24(6), 1251-1261, 2021.

1109 Papale, D., Reichstein, M., Aubinet, M., Canfora, E., Bernhofer, C., Kutsch, W., Longdoz, B., Rambal, S.,
1110 Valentini, R., and Vesala, T.: Towards a standardized processing of Net Ecosystem Exchange
1111 measured with eddy covariance technique: algorithms and uncertainty estimation, *Biogeosciences*,
1112 3(4), 571–583, 2006.

1113 Parton, W. J., Schimel, D. S., Cole, C. V., and Ojima, D. S.: Analysis of factors controlling soil organic
1114 matter levels in Great Plains grasslands, *Soil Science Society of America Journal*, 51(5), 1173–1179,
1115 1987.

1116 Peiro, H., Crowell, S., Schuh, A., Baker, D. F., O’Dell, C., Jacobson, A. R., Chevallier, F., Liu, J., Eldering,
1117 A., and Crisp, D.: Four years of global carbon cycle observed from the Orbiting Carbon Observatory 2
1118 (OCO-2) version 9 and in situ data and comparison to OCO-2 version 7, *Atmospheric Chemistry and
1119 Physics*, 22(2), 1097–1130, 2022.

1120 Peylin, P., Bousquet, P., Le Quéré, C., Sitch, S., Friedlingstein, P., McKinley, G., Gruber, N., Rayner, P.,
1121 Ciais, P.: Multiple constraints on regional CO₂ flux variations over land and oceans, *Global
1122 Biogeochemical Cycles*, 19(1), 2005.

1123 Peylin, P., Law, R. M., Gurney, K. R., Chevallier, F., Jacobson, A. R., Maki, T., Niwa, Y., Patra, P. K.,
1124 Peters, W., and Rayner, P. J.: Global atmospheric carbon budget: results from an ensemble of
1125 atmospheric CO₂ inversions, *Biogeosciences*, 10(10), 6699–6720, 2013.

1126 Peylin, P., Bacour, C., MacBean, N., Leonard, S., Rayner, P., Kuppel, S., Koffi, E., Kane, A., Maignan, F.,
1127 and Chevallier, F.: A new stepwise carbon cycle data assimilation system using multiple data streams
1128 to constrain the simulated land surface carbon cycle, *Geoscientific Model Development*, 9(9), 2016.

1129 Quaife, T., Lewis, P., De Kauwe, M., Williams, M., Law, B. E., Disney, M., and Bowyer, P.: Assimilating
1130 canopy reflectance data into an ecosystem model with an Ensemble Kalman Filter, *Remote Sensing
1131 of Environment*, 112(4), 1347–1364, 2008.

1132 Randerson, J. T., van der Werf, G. R., Giglio, L., Collatz, G. J., and Kasibhatla, P. S.: Global Fire
1133 Emissions Database, Version 3 (GFEDv3. 1), Data set, Oak Ridge National Laboratory Distributed
1134 Active Archive Center, Oak Ridge, Tennessee, USA, 2013.

1135 Raoult, N. M., Jupp, T. E., Cox, P. M., and Luke, C. M.: Land surface parameter optimisation through
1136 data assimilation: the ad-JULES system, *Geosci. Model Dev. Discuss.*, doi: 10.5194, 2016.

1137 Raupach, M. R., Rayner, P. J., Barrett, D. J., DeFries, R. S., Heimann, M., Ojima, D. S., Quegan, S., and
1138 Schimmlus, C. C.: Model–data synthesis in terrestrial carbon observation: methods, data
1139 requirements and data uncertainty specifications, *Global Change Biology*, 11(3), 378–397, 2005.

1140 Rayner, P. J., Scholze, M., Knorr, W., Kaminski, T., Giering, R., and Widmann, H.: Two decades of
1141 terrestrial carbon fluxes from a carbon cycle data assimilation system (CCDAS), *Global
1142 biogeochemical cycles*, 19(2), 2005.

1143 Ricciuto, D. M., King, A. W., Dragoni, D., and Post, W. M.: Parameter and prediction uncertainty in an
1144 optimized terrestrial carbon cycle model: Effects of constraining variables and data record length,
1145 *Journal of Geophysical Research: Biogeosciences*, 116(G1), 2011.

1146 Richardson, A. D., Williams, M., Hollinger, D. Y., Moore, D. J., Dail, D. B., Davidson, E. A., Scott, N. A.,
1147 Evans, R. S., Hughes, H., and Lee, J. T.: Estimating parameters of a forest ecosystem C model with
1148 measurements of stocks and fluxes as joint constraints, *Oecologia*, 164(1), 25–40, 2010.

1149 Sacks, W. J., Schimel, D. S., and Monson, R. K.: Coupling between carbon cycling and climate in a
1150 high-elevation, subalpine forest: a model-data fusion analysis, *Oecologia*, 151(1), 54–68, 2007.

1151 Santaren, D., Peylin, P., Viovy, N., and Ciais, P.: Optimizing a process-based ecosystem model with
1152 eddy-covariance flux measurements: A pine forest in southern France, *Global Biogeochemical Cycles*,
1153 21(2), 2007.

1154 Santaren, D., Peylin, P., Bacour, C., Ciais, P., and Longdoz, B.: Ecosystem model optimization using in
1155 situ flux observations: benefit of Monte Carlo versus variational schemes and analyses of the year-to-
1156 year model performances, *Biogeosciences*, 11(24), 7137–7158, 2014.

1157 Schimel, D. S., Braswell, B. H., Holland, E. A., McKeown, R., Ojima, D. S., Painter, T. H.,... & Townsend,
1158 A. R.: Climatic, edaphic, and biotic controls over storage and turnover of carbon in soils, *Global*
1159 *biogeochemical cycles*, 8(3), 279-293, 1994.

1160 Schimel, D., Stephens, B. B., & Fisher, J. B.: Effect of increasing CO₂ on the terrestrial carbon cycle,
1161 *Proceedings of the National Academy of Sciences*, 112(2), 436-441, 2015.

1162 Schürmann, G. J., Kaminski, T., Köstler, C., Carvalhais, N., Voßbeck, M., Kattge, J., Giering, R.,
1163 Rödenbeck, C., Heimann, M., and Zaehle, S.: Constraining a land-surface model with multiple
1164 observations by application of the MPI-Carbon Cycle Data Assimilation System V1. 0, *Geoscientific*
1165 *Model Development*, 9(9), 2999–3026, 2016.

1166 Sitch, S., Friedlingstein, P., Gruber, N., Jones, S. D., Murray-Tortarolo, G., Ahlström, A., Doney, S. C.,
1167 Graven, H., Heinze, C., and Huntingford, C.: Recent trends and drivers of regional sources and sinks of
1168 carbon dioxide, *Biogeosciences*, 12(3), 653–679, 2015.

1169 Stöckli, R., Rutishauser, T., Dragoni, D., O’keefe, J., Thornton, P. E., Jolly, M., Lu, L., and Denning, A. S.:
1170 Remote sensing data assimilation for a prognostic phenology model, *Journal of Geophysical Research:*
1171 *Biogeosciences*, 113(G4), 2008.

1172 Tarantola, A.: *Inverse problem theory and methods for model parameter estimation*, Society for
1173 industrial and applied mathematics, 2005.

1174 Thum, T., MacBean, N., Peylin, P., Bacour, C., Santaren, D., Longdoz, B., Loustau, D., and Ciais, P.: The
1175 potential benefit of using forest biomass data in addition to carbon and water flux measurements to
1176 constrain ecosystem model parameters: case studies at two temperate forest sites, *Agricultural and*
1177 *Forest Meteorology*, 234, 48–65, 2017.

1178 Todd-Brown, K. E., Randerson, J. T., Post, W. M., Hoffman, F. M., Tarnocai, C., Schuur, E. A., & Allison,
1179 S. D.: Causes of variation in soil carbon simulations from CMIP5 Earth system models and comparison
1180 with observations, *Biogeosciences*, 10(3), 1717-1736, 2013.

1181 Trémolet, Y.: Accounting for an imperfect model in 4D-Var, *Quarterly Journal of the Royal*
1182 *Meteorological Society: A journal of the atmospheric sciences, applied meteorology and physical*
1183 *oceanography*, 132(621), 2483-2504, 2006.

1184 Vermote, E., Justice, C. O., and Bréon, F.-M.: Towards a generalized approach for correction of the
1185 BRDF effect in MODIS directional reflectances, *IEEE Transactions on Geoscience and Remote Sensing*,
1186 47(3), 898–908, 2008.

1187 Wang, Y.-P., Leuning, R., Cleugh, H. A., and Coppin, P. A.: Parameter estimation in surface exchange
1188 models using nonlinear inversion: how many parameters can we estimate and which measurements
1189 are most useful?, *Global Change Biology*, 7(5), 495–510, 2001.

1190 van der Werf, G. R., Randerson, J. T., Giglio, L., Collatz, G. J., Kasibhatla, P. S., and Arellano Jr, A. F.:
1191 Interannual variability in global biomass burning emissions from 1997 to 2004, *Atmospheric*
1192 *Chemistry and Physics*, 6(11), 3423–3441, 2006.

1193 Williams, M., Richardson, A. D., Reichstein, M., Stoy, P. C., Peylin, P., Verbeeck, H., Carvalhais, N.,
1194 Jung, M., Hollinger, D. Y., and Kattge, J.: Improving land surface models with FLUXNET data,
1195 *Biogeosciences*, 6(7), 1341–1359, 2009.

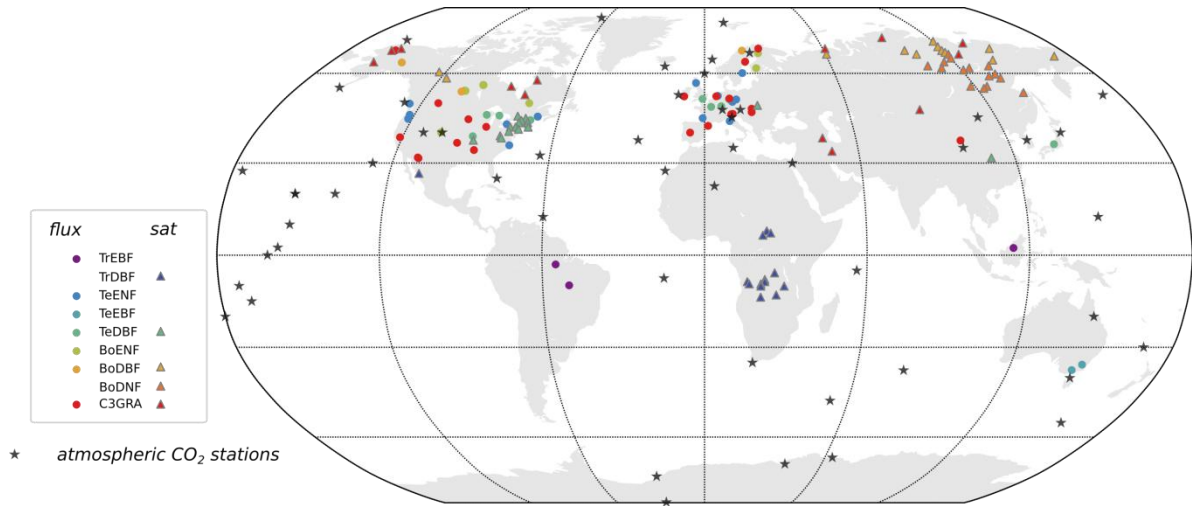
1196 Wutzler, T. and Carvalhais, N.: Balancing multiple constraints in model-data integration: Weights and
1197 the parameter block approach, *Journal of Geophysical Research: Biogeosciences*, 119(11), 2112–2129,
1198 2014.

1199 Zhu, C., Byrd, R. H., Lu, P., and Nocedal, J.: Algorithm 778: L-BFGS-B: Fortran subroutines for large-
1200 scale bound-constrained optimization, *ACM Transactions on mathematical software (TOMS)*, 23(4),
1201 550–560, 1997.

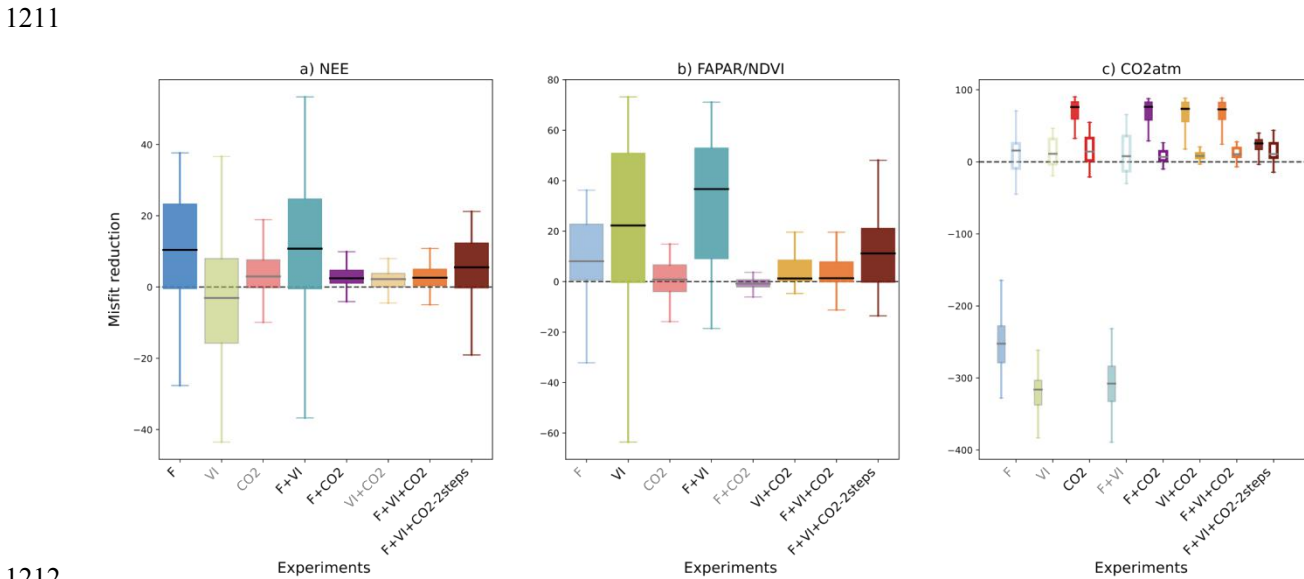
1202 Zobitz, J. M., Moore, D. J., Quaife, T., Braswell, B. H., Bergeson, A., Anthony, J. A., and Monson, R. K.:
1203 Joint data assimilation of satellite reflectance and net ecosystem exchange data constrains
1204 ecosystem carbon fluxes at a high-elevation subalpine forest, *Agricultural and Forest Meteorology*,
1205 195, 73–88, 2014.

1206

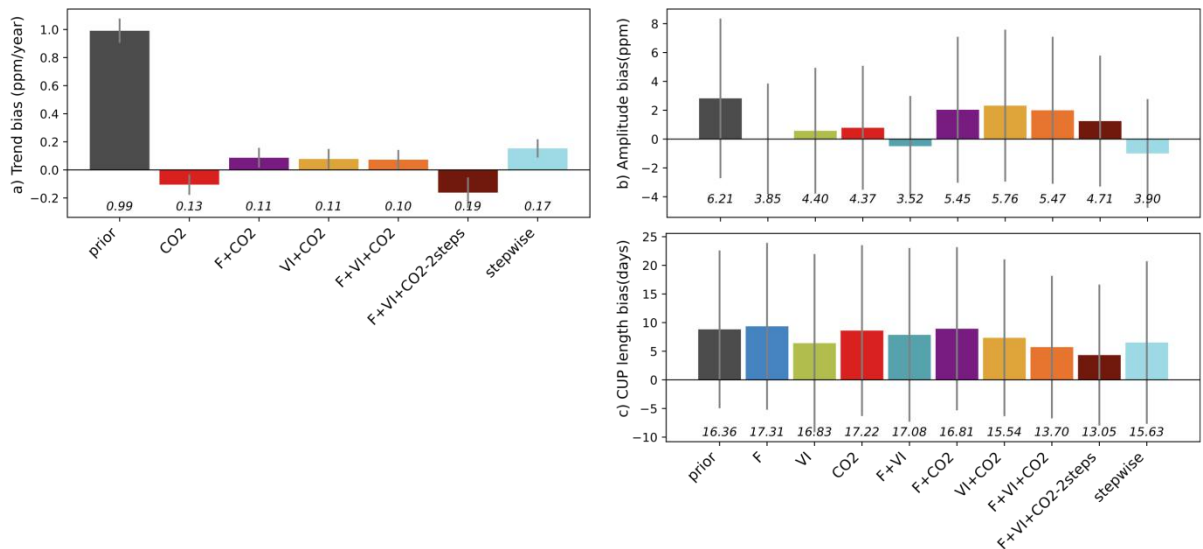
1207



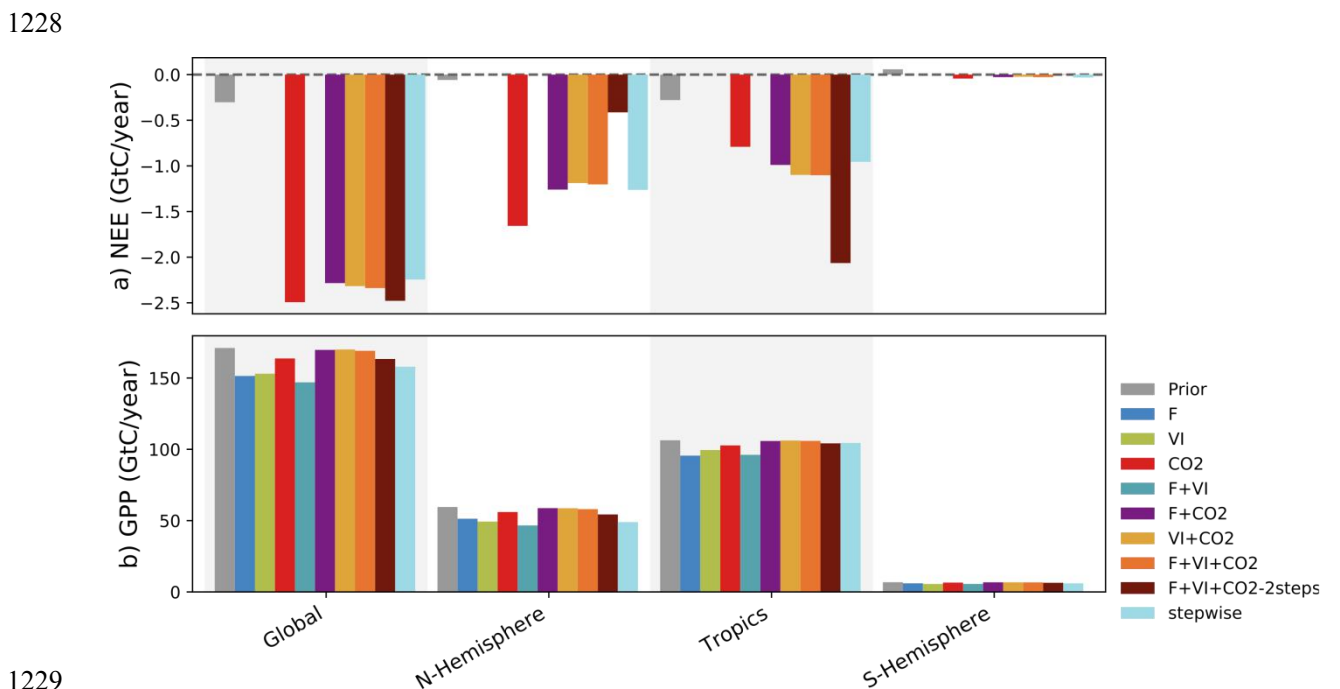
1208
 1209 **Figure 1: Location of the flux tower sites (circles), satellite pixels (triangles), and atmospheric CO₂**
 1210 **stations (black stars) used in this study.**



1212
 1213 **Figure 2: For all data streams, boxplots of the reduction of the model-data mismatch following the**
 1214 **different assimilation experiments. For a given data stream, the assimilation experiments in which**
 1215 **it is involved are labeled in black (x-axis) and the boxplot colors are dark colored; and in gray / light**
 1216 **colors otherwise (back-compatibility check). For the atmospheric CO₂ concentration data at**
 1217 **stations, the misfit reduction is calculated both for the raw (not detrended) data (left solid boxplot**
 1218 **of each assimilation experiment, with colored boxplots) and the detrended data (right white**
 1219 **boxplot of each assimilation experiment).**

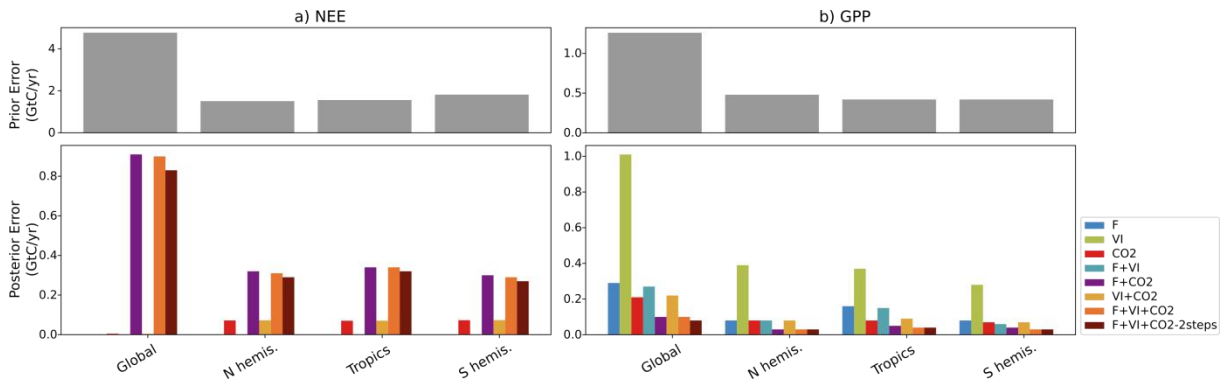


1220
 1221 **Figure 3: Residual biases of the atmospheric CO₂ time series between those measured at stations**
 1222 **and the simulations (prior and optimized for each assimilation experiment), in terms of trend,**
 1223 **magnitude of the seasonal cycle and length of the carbon uptake (CUP). The study results are**
 1224 **compared to those obtained using a sequential approach (Peylin et al., 2016). The bars show for**
 1225 **each quantity the mean bias relative to the measurements over the period 2000-2009. The**
 1226 **standard deviations of the differences between observations and simulations over all stations are**
 1227 **shown as the gray vertical lines, and the RMSD are provided below in italic.**



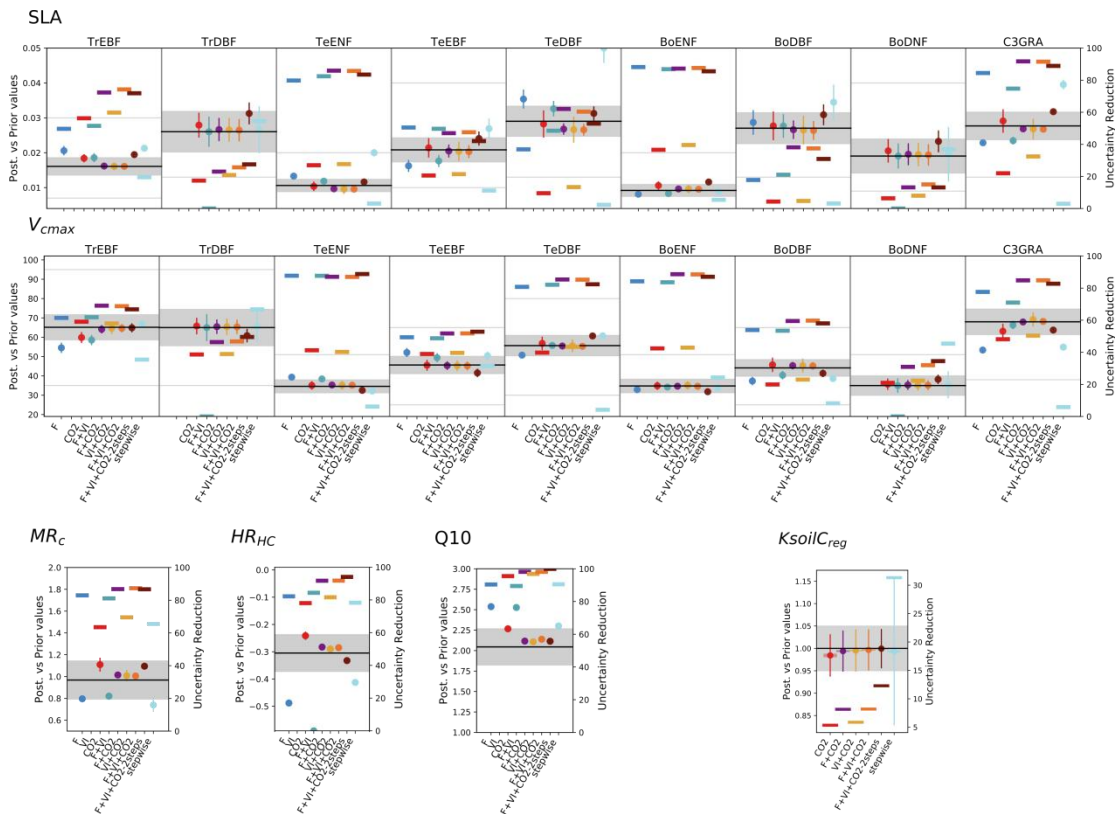
1229
 1230 **Figure 4: Global and regional C budget for NEE and GPP, and for the northern hemisphere (30°N-**
 1231 **90°N), tropics (30°N-30°S) and southern hemisphere (30°S-90°S), regions, for the prior model and**

1232 the model calibrated for the several assimilation experiments. For NEE, only the experiments
 1233 involving atmospheric CO₂ data are shown. The period considered is 2000-2009.



1234
 1235 **Figure 5: For NEE (left) and GPP (right) prior errors (top), and posterior errors obtained for each**
 1236 **assimilation experiment (bottom), over the regions considered. For NEE, only the experiments**
 1237 **involving atmospheric CO₂ data are shown.**

1238



1239
 1240 **Figure 6: Prior and posterior parameter values and uncertainties for a set of optimized parameters**
 1241 **(two PFT-dependent parameters - SLA and V_{cmax} - and four non-PFT dependent). The prior value is**
 1242 **shown as the horizontal black line and the prior uncertainty (standard deviation) as the gray area**
 1243 **encompassing it along the x-axis. For the PFT-dependent parameters, each box corresponds to a**

1244 given PFT; empty boxes indicate that this parameter was not constrained for the corresponding
1245 PFTs. The white zone (non-dashed area) corresponds to the allowed range of variation. The
1246 optimized values are provided for each assimilation experiment (the eight ones considered in this
1247 study and the one from Peylin et al. (2016) – "stepwise"); the corresponding posterior errors are
1248 displayed as the vertical bars. Note that the prior values presented here are those used in this
1249 study, and not those of the stepwise (which are higher/lower for the photosynthesis and
1250 respiration / phenological parameters). For each assimilation experiment is also provided the
1251 uncertainty reduction (right y-axis) as the thick opaque horizontal bars. For *KsoilC_reg*, the
1252 posterior values displayed here correspond to the mean over the ecoregions (without Antarctica)
1253 considered; the semi-transparent horizontal bars on either side of the posterior values correspond
1254 to the standard deviation of the estimates.

1255

1256

1257

Name	Description	Data stream
<u>Photosynthesis</u>		
V_{cmax}	maximum carboxylation rate ($\mu\text{mol}\cdot\text{m}^{-2}\cdot\text{s}^{-1}$)	F, CO2
G_{s,slope}	Ball-Berry slope	F, CO2
T_{opt}	optimal photosynthesis temperature ($^{\circ}\text{C}$)	F, CO2
SLA	specific leaf area ($\text{m}^2\cdot\text{g}^{-1}$)	F, CO2
<u>Soil water availability</u>		
H_{um,cste}	root profile (m^{-1})	F, CO2
<u>Phenology</u>		
LAI_{MAX}	maximum LAI value	F, CO2
K_{pheno,crit}	multiplicative parameter of the threshold that determines the start of the growing season	F, VI, CO2
T_{senes}	temperature threshold for senescence ($^{\circ}\text{C}$)	F, VI, CO2
L_{age,crit}	average critical age of leaves (days)	F, VI, CO2
K_{LAI,happy}	LAI threshold to stop using carbohydrate reserves	F, VI, CO2
<u>Respiration</u>		
Q10	temperature dependency of heterotrophic respiration	F, CO2
HR_{H,c}	Offset of the function for moisture control factor of heterotrophic respiration	F, CO2
MR_c	Offset of the affine relationship between temperature and maintenance respiration	F, CO2
K_{soilC,site}	Multiplicative factor of initial slow and passive carbon pools	F
K_{soilC,reg}	Multiplicative factor of initial slow and passive carbon pools	CO2

1258 **Table 1: List of the ORCHIDEE parameters to be optimized and data streams that constrain them (F**
1259 **for *in situ* flux measurements, VI for normalized satellite NDVI data, CO2 for atmospheric CO₂**
1260 **concentration data).**

1261

1262

experiment name	flux data	NDVI data	atmospheric CO ₂ concentrations	number of optimized parameters	number of observations
F	x			133	150792
VI		x		19	149916
CO2			x	114	6360
F+VI	x	x		152	300708
F+CO2	x		x	182	157152
VI+CO2		x	x	114	156276
F+VI+CO2 F+VI+CO2-2steps	x	x	x	182	307068

1263 **Table 2: Characteristics of the various assimilation experiments (flux data – F, satellite NDVI**
1264 **vegetation index – VI, and atmospheric CO₂ concentration – CO2).**

1265

1266

	NEE	LE	VI	CO2
\mathbf{R}_o	1.75	1.75	0.33	1.22
$E[\mathbf{d}_a^o \cdot \mathbf{d}_b^{oT}]$	1.49	1.49	0.21	1.16
$ratio^B$	1.17	1.17	1.55	1.05
$\mathbf{H}^o \cdot \mathbf{B} \cdot \mathbf{H}^{oT}$	1.45	8.30	0.2	15.17
$E[\mathbf{d}_b^a \cdot \mathbf{d}_b^{oT}]$	0.92	5.45	0.24	6.29
$ratio^B$	1.59	1.52	0.83	2.41
$\mathbf{H}^o \cdot \mathbf{B} \cdot \mathbf{H}^{oT} + \mathbf{R}_o$	2.28	23.63	0.38	15.22
$E[\mathbf{d}_b^o \cdot \mathbf{d}_b^{oT}]$	1.75	22.11	0.31	6.39
$ratio^{BR}$	1.17	1.07	1.23	2.38
$\mathbf{H}^o \cdot \mathbf{A} \cdot \mathbf{H}^{oT}$	0.25	1.82	0.07	3.26
$E[\mathbf{d}_b^a \cdot \mathbf{d}_a^{oT}]$	-0.45	-5.12	-0.15	-2.13
$ratio^A$	-0.56	-0.36	-0.43	-1.53

1267 **Table 3: Consistency diagnostics of the error covariance matrices for the F (using NEE and LE data),**
1268 **VI, and CO2, assimilation experiments. The ratios are calculated with the mathematical**
1269 **expectation term as the denominator.**

1270

	OI		Relative DFS	
	1-step	2-step	1-step	2-step
flux	0.000586	0.000577	74.65	76.9
NDVI	0.000048	0.000048	11.12	11.68
CO2	0.002654	0.002035	14.23	11.42

1271 **Table 4: Observation influence and relative DFS statistics of each data stream for the joint**
1272 **assimilation experiments F+VI+CO2 and F+VI+CO2-2steps.**

1273